

---

# 18 Radar Monitoring of Volcanic Activities

*Zhong Lu and Daniel Dzurisin*

## CONTENTS

18.1	Introduction.....	421
18.2	Radar.....	422
18.3	Synthetic Aperture Radar.....	424
18.4	Interferometric Synthetic Aperture Radar.....	425
18.4.1	InSAR Processing Flow.....	425
18.5	InSAR Products and Their Applications to Volcanoes.....	432
18.5.1	SAR Intensity Image.....	432
18.5.2	InSAR Deformation Image and Source Parameters Derived from Modelling.....	434
18.5.3	InSAR Coherence Image.....	435
18.5.4	Digital Elevation Model.....	437
18.6	Multi-Interferogram InSAR.....	439
18.7	Conclusion.....	441
	Acknowledgements.....	441
	References.....	441

## 18.1 INTRODUCTION

Earth is home to about 1500 volcanoes that have erupted in the past 10,000 years, and today volcanic activity affects the lives and livelihoods of a rapidly growing number of people around the globe. About 20 volcanoes are erupting on Earth at any given time; 50–70 erupt each year, and about 160 erupt each decade. Impressive as these statistics are, they do not include a large but unspecified number of volcanic vents along submarine midocean ridges that girdle the globe (Smithsonian Institution, Global Volcanism Program, <http://www.volcano.si.edu/faq.cfm#q3>).

The nature of eruptive activity ranges from the quiet outpouring of fluid lava on the ocean floor and in places like Hawaii (<http://hvo.wr.usgs.gov/>) to the explosive ejection of volcanic ash, pumice and other fragmental material at volcanoes like Mount Fuji (Japan), Mount St. Helens (United States), Chaitén (Chile) and others along the Pacific Ring of Fire and elsewhere. Less frequent, larger events, like the 1912 eruption of Novarupta–Mount Katmai (Alaska) (Hildreth and Fierstein 2012) and the 1991 eruption of Mount Pinatubo (Philippines) (Newhall and Punongbayan 1996), produce local and regional impacts that can last for decades, and shorter-term effects on the average global temperature. At the extreme end of the spectrum, it has been suggested that a catastrophic eruption at Lake Toba on the Indonesian island of Sumatra about 74,000 years ago caused a decade-long ‘volcanic winter’, resulting in a genetic bottleneck that profoundly affected the course of human evolution—an idea that remains plausible but controversial (Robock 2013 and references therein).

The products of volcanic eruptions also vary widely, giving rise to a large range of associated hazards (Myers et al. 2008). Explosive eruptions produce ballistic ejecta (solid and molten rock fragments) that can impact the surface up to several kilometres away from the vent. Smaller fragments are carried upward in eruption columns that sometimes reach the stratosphere, forming eruption clouds that pose a serious hazard to aircraft. Large eruption clouds can extend hundreds to

thousands of kilometres downwind, resulting in ash fall over large areas. Heavy ash fall can collapse buildings, and even minor amounts can cause significant damage and disruption to everyday life. Volcanic gases in high concentrations can be deadly. In lower concentrations, they contribute to health problems and acid rain, which causes corrosion and harms vegetation. Lava flows and domes extruded during mostly non-explosive eruptions can inundate property and infrastructure, and create flood hazards by damming streams or rivers. Pyroclastic flows – high-speed avalanches of hot pumice, ash, rock fragments and gas – can move at speeds in excess of 100 km/h and destroy everything in their path. In some cases, gravitational collapse of an unstable volcanic edifice results in a devastating debris avalanche; the most famous example is the 1980 debris avalanche at Mount St. Helens, which extended more than 20 km down the North Fork Toutle River Valley. Debris flows and lahars (volcanic mudflows) triggered by eruptions inundate valleys for distances approaching 100 km, causing long-term ecological impacts and increased flood hazards.

Assessment, monitoring and preparedness are three keys to mitigating the adverse impacts of volcanic activity. Radar can play a direct role in helping to monitor volcanoes and assess hazards, both during periods of unrest and during ensuing eruptions. For example, interferometric synthetic aperture radar (InSAR) images can be used to distinguish between deep and shallow sources of volcano deformation, and between the deformation pattern caused by magma accumulation in a subsurface reservoir and that caused by upward intrusion of a magma-filled dyke from the reservoir towards the surface. During the course of an eruption when the volcano is obscured by clouds or darkness, Synthetic Aperture Radar (SAR) intensity images might be the only means available to track hazardous developments, such as the emergence of a gravitationally unstable lava dome. Ground-based Doppler radars can track volcanic ash clouds and provide short-term warnings to aircraft and to areas downwind that are likely to receive ash fall. Insights gained from radar studies also can contribute to improved public awareness and preparedness for volcanic activity through proactive public information programmes. For additional information about volcano hazards, hazard assessments and eruption preparedness, see <http://volcanoes.usgs.gov/>.

## 18.2 RADAR

The term *radar* is derived from ‘radio detection and ranging’, a phrase that encapsulates some of radar’s essential characteristics and capabilities. Radar systems make use of the radio and microwave portion of the electromagnetic spectrum, with wavelengths ranging from a few millimetres to 100 m or more. Most volcano applications, including SAR and InSAR, make use of wavelengths ranging from a few centimetres to a few tens of centimetres. All radar systems employ a radio transmitter that sends out a beam of microwaves either continuously or in pulses. By measuring the time it takes radio waves travelling at the speed of light to make the round trip from the radar to a target and back, a tracking radar system can determine the distance to the target. If the target is moving with respect to the radar, its velocity can be determined from the frequency of the return signal, which differs from that of the transmitted signal as a result of the Doppler effect. The distance to the target, strength of the return signal and Doppler shift are three fundamental parameters provided by tracking radars. Because of these capabilities, tracking radars are essential tools for air traffic control and weather monitoring.

A typical tracking radar employs a scanning strategy in which the beam sweeps through a range of azimuth and elevation angles in order to map a volume of interest. For example, the radar might transmit pulses while rotating 360° in azimuth at a fixed elevation angle, and then repeat the scan at progressively higher or lower elevation angles. Return echoes from targets are received by the radar antenna and processed by the receiver. Once the radar sweeps through all elevation slices, a volume scan is complete, which provides a three-dimensional view of the airspace around the radar site. Tracking radars equipped with Doppler capability, such as those used for air traffic control, can determine both the location and speed of targets (aircraft) within their range. Weather radars take advantage of the fact that the strength of the return signal depends on the size, density, state

(e.g. solid hail and liquid rain) and shape of scatterers in the beam's path. Based on empirical relationships, the approximate rainfall rate at the ground can be estimated from observations made by weather radar (e.g. <https://radar.weather.gov>). Weather radars equipped with Doppler capability can peer inside thunderstorms and determine if there is rotation in the cloud, which often is a precursor to the development of tornadoes.

Two characteristics of radar that are important for volcano monitoring are (1) unlike optical and infrared systems that are inherently passive (i.e. they rely on natural reflected energy or radiated energy originating at the source), radar is an active sensor that provides its own illumination, and (2) owing to their longer wavelength, radar signals penetrate water clouds, diffuse ash clouds and sparse to moderate vegetation better than visible light, enabling limited 'see-through' capability for objects that are opaque at optical wavelengths. Because radar is an active microwave system, it is equally effective in darkness and daylight, and during bad weather or good. This is a tremendous advantage for volcano monitoring, which requires round-the-clock operations during periods of unrest.

Ground-based Doppler radars have been utilized to detect and track volcanic ash clouds (Harris and Rose 1983; Rose et al. 1995; Dubosclard et al. 1999; Lacasse et al. 2004; Houlié et al. 2005; Tupper et al. 2005; Marzano et al. 2006), which can pose a hazard to buildings, infrastructure, human health and aviation systems (Rose 1977; Miller and Casadevall 2000). Figure 18.1 shows time-series images of a developing ash cloud during the 2009 eruption at Redoubt volcano, Alaska

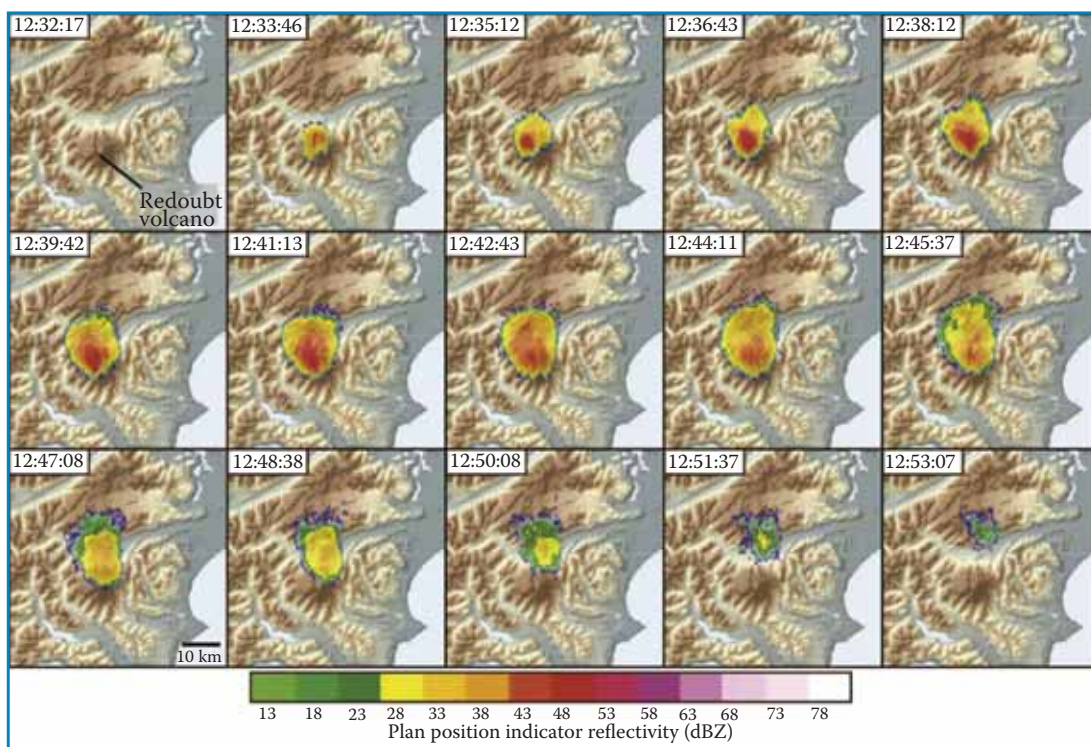


**FIGURE 18.1** Sequence of radar reflectivity images at an altitude of 7.9 km above sea level over Redoubt volcano, Alaska, from a Doppler weather radar located about 82 km east of the volcano. The images show the growth and decline of an eruption cloud on 23 March 2009. Times are in Universal Time Coordinated for starts of volume scans, each of which take 90 seconds to complete. The colour bar at the bottom shows reflectivity values in decibels relative to Z (dBZ), a unit commonly used in weather radar to compare the equivalent reflectivity ( $Z$ ) of a radar signal scattered from a remote object (volcanic ash, in this case) with the return from a droplet of rain with a diameter of 1 mm. For weather clouds, dBZ values can be converted to estimates of rainfall rate using an empirical formula. In this case, the greater dBZ values (warmer colours) correspond to denser parts of the ash cloud. (Modified from Schneider, D., and Hoblitt, R., *J. Volcanol. Geotherm. Res.*, 259, 133–144, 2013.)

(Schneider and Hoblitt 2013). The images show the extent and radar reflectivity of the cloud at an altitude of 7.9 km above sea level. The nearly circular cloud was characterized by a high reflectivity core and lasted at detectable levels for about 20 minutes (Schneider and Hoblitt 2013).

An imaging radar aboard the German Space Agency's TerraSAR-X satellite was used to track the growth, destruction and regrowth of a lava dome at Mount Cleveland volcano in the central Aleutian Islands, Alaska, during 2011–2013 (Lu and Dzurisin 2014, chap. 6, sect. 6.15.5). Mount Cleveland is remote, difficult to access and often obscured by clouds, so the SAR observations provided timely information about the eruption that would not have been available otherwise. Satellite SAR imagery provided similar information that aided hazard assessments during recent eruptions at the Merapi (2013) and Sinabung (2013–2014 ongoing) volcanoes in Indonesia (Smithsonian Institution Global Volcanism Program, <http://volcano.si.edu/>).

### 18.3 SYNTHETIC APERTURE RADAR

SAR is an imaging radar system designed, as the name implies, to take advantage of a large 'synthetic' antenna to produce images of much better resolution than would be possible otherwise. SAR systems operate on the same principles as Doppler radars, but have additional capability to distinguish among return signals from individual resolution elements within a target footprint. SARs are side looking, that is, they direct signals to the side of their path across the surface rather than straight down. As a result, the arrival path of the radar signal is oblique to the surface being imaged. Return signals from near-range parts of the target (the part closest to the ground track of the radar) generally arrive back at the radar sooner than return signals from far-range areas, so the relationship between round-trip travel time and range can be used to organize return signals in the across-track, or range, direction. In the along-track, or azimuth, direction, the Doppler principle comes into play. Signals returned from areas that are ahead of the radar as it travels along its path are shifted to slightly higher frequencies, while returns from trailing areas are shifted to slightly lower frequencies. An imaging radar uses the relationship between return signal frequency and relative velocity between radar and target to organize return signals in the azimuth direction. In this way, the returns from each resolution element on the ground can be assigned unique coordinates in range and azimuth. The resulting data can be processed into an image of the target area, which contains information about topography and radar reflective properties of the surface.

SAR systems take advantage of the fact that each point along the ground swath is illuminated for an extended period of time while the footprint of the radar beam moves across it. The resolution of an imaging radar is inversely proportional to the size (aperture) of the antenna, so a SAR is capable of much better resolution than is possible with a real aperture radar. Conceptually, a SAR image processor makes use of this fact to 'synthesize' a large virtual antenna, and thus achieves much higher spatial resolution than is practical with a real aperture radar. Most SAR systems designed for Earth orbit use an antenna that is 1–4 m wide and 10–15 m long, with a look angle in the range of 10°–60°, to illuminate a footprint 50–150 km wide in the range direction and 5–15 km wide in the azimuth direction. Such a SAR system is capable of producing a ground resolution of 1–10 m in azimuth and 1–20 m in range, which is an improvement by about three orders of magnitude over a comparable real aperture system. Because a SAR actively transmits and receives signals backscattered from the target area, and because radar wavelengths are mostly unaffected by weather clouds, a SAR can operate effectively during day and night under most weather conditions to produce images at times and under conditions that render most optical imaging systems useless for surface observations.

Using a sophisticated image processing technique called SAR processing (Curlander and McDonough 1991; Bamler and Hartl 1998; Henderson and Lewis 1998; Rosen et al. 2000; Massonnet and Souyris 2008), both the intensity and phase of the signal backscattered from each ground resolution element can be calculated and portrayed as part of a complex-valued SAR image. The intensity of a resulting single-look complex (SLC) image is controlled primarily by terrain

slope, surface roughness and surface relative permittivity. Note that *dielectric constant* is the historical term often used to describe this property, but *surface relative permittivity* is more precise and currently accepted by the Institute of Electrical and Electronics Engineers (IEEE) Standards Board (IEEE Standard Definitions of Terms for Radio Wave Propagation 1997). The phase component is controlled mainly by the round-trip travel time from SAR to ground, which is affected by atmospheric conditions (water vapour in the troposphere slows the speed of electromagnetic waves, and electron density in the ionosphere shortens the propagation path) and by interaction of the radar signal with the ground surface.

## 18.4 INTERFEROMETRIC SYNTHETIC APERTURE RADAR

InSAR involves the use of two or more SAR images of the same area to extract the land surface topography plus any surface deformation that might have occurred during the interval between image acquisitions. The images can be created by spatially or temporally separated SARs (i.e. two SARs operating at the same time at slightly different locations, or a single SAR that images the same target area from similar vantage points at two different times). The spatial separation between two SAR antennas is called the baseline. The two antennas can be mounted on a single platform for simultaneous interferometry. This is the usual implementation for aircraft and space-borne systems such as the Topographic SAR (TOPSAR) and Shuttle Radar Topography Mission (SRTM) systems (Farr et al. 2007), which are used to generate digital elevation models (DEMs). Alternatively, InSAR images can be created by using a single antenna on an airborne or space-borne platform in nearly identical repeating flight paths or orbits for repeat-pass interferometry (Gray and Farris-Manning 1993; Massonnet and Feigl 1998). For the latter case, even though the antennas do not illuminate the same area at the same time, the two sets of signals recorded during the two passes will be highly correlated if the scattering properties of the ground surface remain undisturbed during the time between image acquisitions. This is the typical implementation for past and present space-borne sensors, such as the U.S. Seasat and Shuttle Imaging Radar-C (SIR-C); European Remote Sensing Satellites (ERS-1 and ERS-2), Environmental Satellite (Envisat) and Sentinel-1A/B; Canadian Radar Satellite (Radarsat-1 and Radarsat-2); and Japanese Earth Resources Satellite (JERS-1) and Advanced Land Observing Satellite (ALOS) and ALOS-2 – all of which operate at wavelengths ranging from a few centimetres (X-band and C-band) to tens of centimetres (L-band) (Table 18.1). This configuration enables InSAR measurements of surface deformation with millimetre to centimetre precision at a spatial resolution of a few tens of metres over a large region.

### 18.4.1 INSAR PROCESSING FLOW

A SAR image represents the intensity and phase of the reflected (or backscattered) signal from each ground resolution element in the form of a complex-valued data matrix (Figure 18.2). Generating an interferogram requires two SLC SAR images. Neglecting phase shifts induced by the transmitting and receiving antenna and SAR processing algorithms, the phase value of a pixel in an SLC SAR image (Figure 18.2b) can be represented as

$$\phi_1 = W \left\{ -\frac{4\pi}{\lambda} r_1 + \varepsilon_1 \right\} \quad (18.1)$$

where  $r_1$  is the apparent range distance (including possible atmospheric delay) from the antenna to the ground target,  $\lambda$  is the radar wavelength,  $\varepsilon_1$  is the sum of phase shifts due to the interaction between the incident radar wave and scatterers within the resolution cell and  $W\{\}$  is a wrapping operator so that the observed  $\phi_1$  is wrapped into the interval of  $(-\pi, \pi)$ . Because the backscattering phase ( $\varepsilon_1$ ) is a randomly distributed (unknown) variable, the phase value ( $\phi_1$ ) in a single SAR image

**TABLE 18.1**  
**Satellite SAR Sensors Capable of InSAR Mapping**

Mission	Agency	Period of Operation	Orbit Repeat Cycle (days)	Band/Frequency (GHz)	Wavelength (cm)	Incidence Angle (°) at Swath Centre	Resolution (m)
Seasat	NASA	June 1978–October 1978	17	L-band/1.275	23.5	23	25
ERS-1	ESA	July 1991–March 2000	3, 168 and 35 <sup>a</sup>	C-band/5.3	5.66	23	30
JERS-1	JAXA	February 1992–October 1998	44	L-band/1.275	23.5	39	20
ERS-2	ESA	April 1995–July 2011	35 and 3 <sup>b</sup>	C-band/5.3	5.66	23	30
Radarsat-1	CSA	November 1995–2013	24	C-band/5.3	5.66	10–60	10–100
Envisat	ESA	March 2002–April 2012	35 and 30 <sup>c</sup>	C-band/5.331	5.63	15–45	20–100
ALOS	JAXA	January 2006–May 2011	46	L-band/1.270	23.6	8–60	10–100
TerraSAR-X	DLR	June 2007–present	11	X-band/9.65	3.11	20–55	0.24–260
Radarsat-2	CSA	December 2007–present	24	C-band/5.405	5.55	10–60	3–100
COSMO-SkyMed	ASI	June 2007–present	1, 4, 5, 7, 8, 9, 12 and 16 <sup>d</sup>	X-band/9.6	3.12	20–60	1–100
RISAT-2	ISRO	April 2009–present	14	X-band/9.59	3.13	20–45	1–8
TanDEM-X <sup>e</sup>	DLR	June 2010–present	11	X-band/9.65	3.11	20–55	1–16
RISAT-1	ISRO	April 2012–present	25	C-band/5.35	5.61	15–50	3–50
Sentinel-1A	ESA	April 2014–present	12	C-band/5.405	5.55	20–47	5–40
ALOS-2	JAXA	May 2014–present	14	L-band/1.2575 (and more)	23.9 (and more)	8–70	1–100
Sentinel-1B	ESA	April 2016–present	12	C-band/5.405	5.55	20–47	5–40

*Note:* ASI, Italian Space Agency; CSA, Canadian Space Agency; ESA, European Space Agency; ISRO, Indian Space Research Organization; JAXA, Japan Aerospace Exploration Agency; RISAT-1, Radar Imaging Satellite-1; RISAT-2, Radar Imaging Satellite-2.

<sup>a</sup> To accomplish various mission objectives, the ERS-1 repeat cycle was 3 days from 25 July 1991 to 1 April 1992 and from 13 December 1993 to 9 April 1994; 168 days from 10 April 1994 to 20 March 1995; and 35 days at other times.

<sup>b</sup> The ERS-2 repeat cycle was mainly 35 days. During the few months before the end of the mission, the ERS-2 repeat cycle was changed to 3 days to match the 3-day-repeat ERS-1 phases in 1991–1992 and 1993–1994.

<sup>c</sup> The Envisat repeat cycle was 35 days from March 2002 to October 2010, and 30 days from November 2010 to April 2012.

<sup>d</sup> A constellation of four satellites, each of which has a repeat cycle of 16 days, can collectively produce repeat-pass InSAR images at intervals of 1, 4, 5, 7, 8, 9 and 12 days, respectively.

<sup>e</sup> TerraSAR add-on for digital elevation measurements.

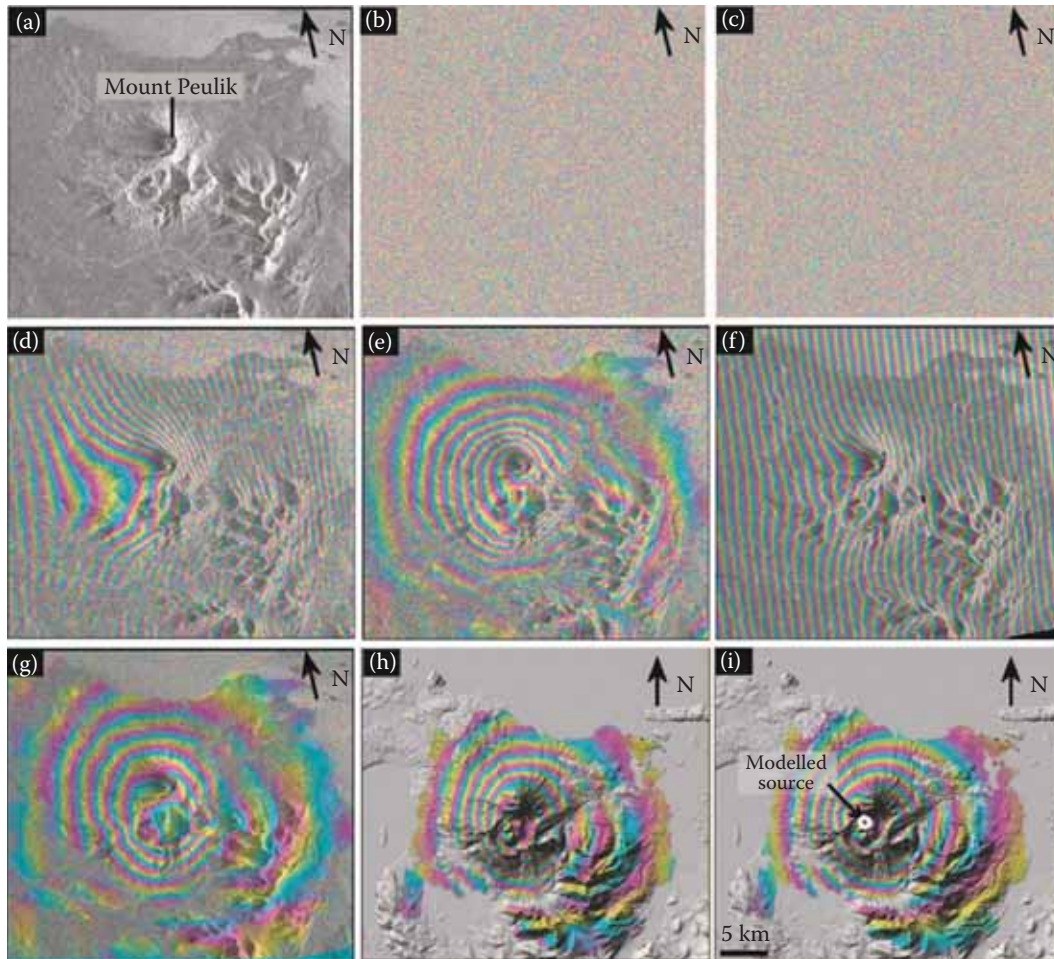


**FIGURE 18.2** (a) Amplitude component of an ERS-1 SAR image acquired on 4 October 1995 over Mount Peulik volcano, Alaska. (b) Phase component of the SLC SAR image corresponding to the amplitude image in (a). (c) Phase component of an ERS-2 SAR image of Mount Peulik acquired on 9 October 1997. The amplitude component is similar to that in (a) and therefore is not shown. The phase values represented in (b) and (c) look spatially random but nonetheless contain useful information after InSAR processing. (d) Original interferogram formed by differencing the phase values of two co-registered SAR images, (b) and (c). The resulting InSAR image contains fringes produced by the differing viewing geometries, topography, any atmospheric delays, surface deformation and noise. The perpendicular component of the InSAR baseline is 35 m in this case. (e) Flattened interferogram produced by removing the effect of a flat Earth surface from the original interferogram (d). (f) Simulated interferogram representing the contribution of topography in the original interferogram (d) using knowledge of the InSAR imaging geometry and a DEM. (g) Topography-removed interferogram produced by subtracting the simulated interferogram (f) from the original interferogram (d). The resulting interferogram contains fringes produced by surface deformation, any atmospheric delays and noise. (h) Georeferenced topography-removed interferogram overlaid on a shaded relief image produced from a DEM. The concentric pattern of fringes indicates ~17 cm of uplift centred on the volcano, which occurred during an aseismic inflation episode between 1996 and 1998 prior to a strong earthquake swarm ~30 km to the northwest (Lu et al. 2002b). (i) Model interferogram produced using a best-fit inflationary point source at ~6.5 km depth with a volume change of ~0.043 km<sup>3</sup> overlaid on the shaded relief image (compare to (h)). Each interferometric fringe (full-colour cycle or band) represents 360° of phase change (b–f), or 2.83 cm of range change (g–i) between the ground and the satellite along the satellite look direction. Areas of loss of InSAR coherence are uncoloured in (h) and (i).

cannot be used to calculate the range ( $r_1$ ) and is of no practical use. However, assume that a second SLC SAR image of the same area (with the phase image shown in Figure 18.2c) is obtained at a different time with a phase value represented by

$$\phi_2 = W \left\{ -\frac{4\pi}{\lambda} r_2 + \varepsilon_2 \right\} \quad (18.2)$$

Note that, by itself, the second SAR image cannot provide useful range information ( $r_2$ ) either.

An interferogram (Figure 18.2d) is created by co-registering two SAR images and differencing the corresponding phase values (Figure 18.2b,c) on a pixel-by-pixel basis. The phase value of the resulting interferogram (Figure 18.2d) is

$$\phi = \phi_1 - \phi_2 = W \left\{ -\frac{4\pi(r_1 - r_2)}{\lambda} + (\varepsilon_1 - \varepsilon_2) \right\} \quad (18.3)$$

The fundamental assumption in repeat-pass InSAR is that the scattering characteristics of the ground surface do not change during the interval between image acquisitions. The degree of change can be quantified by the interferometric coherence value, which is discussed in Section 18.5.3. Assuming that the interactions between radar waves and scatterers remain the same (i.e.  $\varepsilon_1 = \varepsilon_2$ ), the interferometric phase value can be expressed as

$$\phi = W \left\{ -\frac{4\pi(r_1 - r_2)}{\lambda} \right\} \quad (18.4)$$

Typical values for the range difference, ( $r_1 - r_2$ ), are from a few metres to several hundred metres. The SAR wavelength ( $\lambda$ ) is of the order of several centimetres. Because the measured interferometric phase value ( $\phi$ ) is modulated by  $2\pi$ , ranging from  $-\pi$  to  $\pi$ , there is an ambiguity of many cycles (i.e. numerous  $2\pi$  values) in the interferometric phase value. Therefore, the phase value of a single pixel in an interferogram is of no practical use. However, the change in range difference,  $\delta(r_1 - r_2)$ , between two neighbouring pixels that are a few metres apart is normally much smaller than the SAR wavelength. So the phase difference between two nearby pixels,  $\delta\phi$ , can be used to infer the range difference ( $r_1 - r_2$ ) to a precision that is a small fraction of the radar wavelength. This explains how the InSAR technique can determine range changes to within a few millimetres or centimetres based on observed phase differences between two co-registered images.

The phase (or range distance difference) in the original interferogram (Figure 18.2d) contains contributions from both the topography and any possible ground surface deformation. Therefore, the topographic contribution needs to be removed from the original interferogram in order to derive a deformation map. The most common procedure is to use an existing DEM and knowledge of the InSAR imaging geometry to produce a synthetic interferogram that represents the topographic effect and subtract it from the interferogram to be studied (Massonnet and Feigl 1998; Rosen et al. 2000). This is the so-called two-pass InSAR technique. Alternatively, a synthetic interferogram that represents the topographic contribution can be produced from a different interferogram of the same area that is either insensitive to deformation or does not span the deformation episode (if known by some other means). The procedures are then called three-pass or four-pass InSAR (Zebker et al. 1994). Because the two-pass InSAR method is commonly used for deformation mapping, we explain briefly how to simulate the effect of topography in an InSAR image based on an existing DEM.

Two steps are required to simulate a topography-only interferogram based on a DEM. In the first step, the DEM needs to be resampled to project heights from a map coordinate into the appropriate

radar geometry via geometric simulation of the imaging process. The InSAR imaging geometry is shown in Figure 18.3. The InSAR system acquires two images of the same scene with SAR platforms located at  $A_1$  and  $A_2$ . The baseline, defined as the vector from  $A_1$  to  $A_2$ , has a length  $B$  and is tilted with respect to the horizontal by angle  $\alpha$ . The slant range  $r$  from the SAR to a ground target  $T$  with an elevation value  $h$  is linearly related to the measured phase values in the SAR images by Equations 18.1 and 18.2. The look angle from  $A_1$  to the ground point  $T$  is  $\theta_1$ . For each ground resolution cell at ground range  $r_g$  with elevation  $h$ , the slant range value ( $r_1$ ) should satisfy

$$r_1 = \sqrt{(H + R)^2 + (R + h)^2 - 2(H + R)(R + h) \cos\left(\frac{r_g}{R}\right)} \quad (18.5)$$

where  $H$  is the SAR altitude above a reference Earth surface, which is assumed to be a sphere with radius  $R$ . The radar slant range and azimuth coordinates are calculated for each point in the DEM. This set of coordinates forms a non-uniformly sampled grid in SAR coordinate space. The DEM

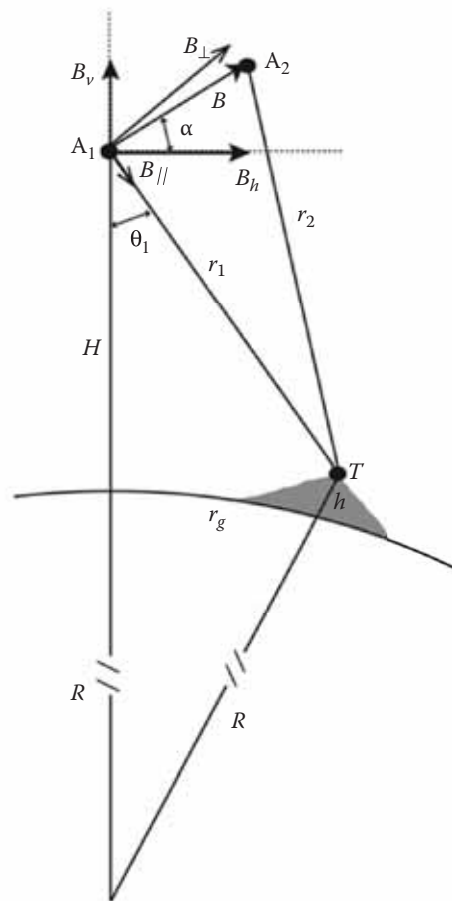


**FIGURE 18.3** Schematic showing InSAR imaging geometry. Two SAR images of the same target area are acquired from vantage points  $A_1$  and  $A_2$ . The baseline  $B$  (the spatial distance between SAR antennas  $A_1$  and  $A_2$ ) is tilted with respect to the horizontal by angle  $\alpha$ , and can be represented by a pair of horizontal ( $B_h$ ) and vertical ( $B_v$ ) components, or by a pair of parallel ( $B_{||}$ ) and perpendicular ( $B_{\perp}$ ) components. The slant range distances from  $A_1$  and  $A_2$  to a ground target  $T$  with elevation above the ground surface  $h$  are  $r_1$  and  $r_2$ , respectively. The altitude of  $A_1$  is  $H$ , and the ground range from  $A_1$  to  $T$  is  $r_g$ . The look angle from  $A_1$  to  $T$  is  $\theta_1$ . The radius of the spherical Earth is  $R$ .

height data are then resampled into a uniform grid in the radar coordinates using the values from the non-uniform grid.

In the second step, the precise look angle from  $A_1$  to ground target  $T$  at ground range  $r_g$ , slant range  $r_1$  and elevation  $h$  is calculated:

$$\theta_1 = \arccos \left[ \frac{(H + R)^2 + r_1^2 - (R + h)^2}{2(H + R)r_1} \right] \quad (18.6)$$

Finally, the interferometric phase value due to the topographic effect at target  $T$  can be calculated:

$$\phi_{\text{dem}} = -\frac{4\pi}{\lambda}(r_1 - r_2) = \frac{4\pi}{\lambda} \left( \sqrt{r_1^2 - 2(B_h \sin \theta_1 - B_v \cos \theta_1)r_1 + B^2} - r_1 \right) \quad (18.7)$$

where  $B_h$  and  $B_v$  are horizontal and vertical components of the baseline  $B$  (Figure 18.3).

Figure 18.2e shows the simulated topographic effect in the original interferogram (Figure 18.2d) calculated using an existing DEM and the InSAR imaging geometry (Figure 18.3). Removing the topographic effect (Figure 18.2e) from the original interferogram (Figure 18.2d) results in an interferogram that represents ground surface deformation during the time interval between image acquisitions, plus measurement noise (Figure 18.2f). The resulting phase value can be written as

$$\phi_{\text{def}} = W\{\phi - \phi_{\text{dem}}\} \quad (18.8)$$

In common practice, an ellipsoidal Earth surface characterized by its major axis,  $e_{\text{maj}}$ , and minor axis,  $e_{\text{min}}$ , is used instead of a spherical Earth model. The radius of the Earth at the imaged area is then

$$R = \sqrt{(e_{\text{min}} \sin \beta)^2 + (e_{\text{maj}} \cos \beta)^2} \quad (18.9)$$

where  $\beta$  is the latitude of the centre of the imaged region.

If  $h$  is taken as zero, the procedure outlined in Equations 18.5 through 18.9 will remove the effect of an ellipsoidal Earth surface on the interferogram. This results in a flattened interferogram, in which phase values can be approximated as

$$\phi_{\text{flat}} = -\frac{4\pi}{\lambda} \frac{B \cos(\theta_1 - \alpha)}{r_1 \sin \theta_1} h + \phi_{\text{def}} = -\frac{4\pi}{\lambda} \frac{B_{\perp}}{H \tan \theta_1} h + \phi_{\text{def}} \quad (18.10)$$

where  $B_{\perp}$  is the perpendicular component of the baseline with respect to the incidence angle  $\theta_1$  (Figure 18.3). Removing the effect of an ellipsoidal Earth surface from the original interferogram (Figure 18.2d) results in the flattened interferogram shown in Figure 18.2g.

If  $\phi_{\text{def}}$  in Equation 18.10 is negligible (i.e. no deformation) or can be removed from an independent source (Lu et al. 2013), the phase value in Equation 18.10 can be used to calculate the surface height  $h$ . This explains how InSAR can be used to produce an accurate, high-resolution DEM for a large region. If the primary goal is to produce a DEM but the interferogram is also affected by ground deformation (i.e.  $\phi_{\text{def}}$  is not negligible), the deformation effect can be calculated from a second interferogram that is less sensitive to topography, and then removed from the first interferogram (Lu and Dzurisin 2014).

For the ERS-1/2 satellites,  $H$  is about 800 km,  $\theta_1$  is about  $23^\circ \pm 3^\circ$ ,  $\lambda$  is 5.66 cm and  $B_\perp$  should be less than 1100 m for a coherent interferogram. Therefore, Equation 18.10 can be approximated as

$$\phi_{flat} \approx -\frac{2\pi}{9600} B_\perp h + \phi_{def} \quad (18.11)$$

For an interferogram with  $B_\perp$  of 100 m, 1 m of topographic relief produces a phase value of about  $4^\circ$ . However, producing the same phase value requires only 0.3 mm of surface deformation.  $\phi_{flat}$  in Equation 18.11 can be considered a function of two variables,  $h$  and  $\phi_{def}$ . The coefficient (i.e.  $2\pi B_\perp/9600$ ) for  $h$  is much less than 1, while the coefficient for  $\phi_{def}$  is equal to 1. So for a given imaging geometry, the interferogram phase value is much more sensitive to changes in topography (i.e. surface deformation  $\phi_{def}$ ) than to the topography itself ( $h$ ). This explains why repeat-pass InSAR is capable of mapping surface deformation with millimetre to centimetre precision.

With the two-pass InSAR technique, DEM errors can be incorrectly mapped into apparent surface deformation. The effect is characterized by the so-called ‘altitude of ambiguity’, which is the amount of DEM error required to generate one interferometric fringe in a topography-removed interferogram (Massonnet and Feigl 1998). Because the altitude of ambiguity is inversely proportional to the perpendicular baseline  $B_\perp$ , interferometric pairs with small baselines are better suited for deformation analysis. Conversely, pairs with larger baselines (within the constraint imposed by coherence; see Section 18.5.2) are preferable for DEM generation.

One significant error source in repeat-pass InSAR deformation measurements is inhomogeneity in the atmosphere that results in path-delay anomalies (Lu and Dzurisin 2014). Differences in atmospheric water vapour content (and temperature and pressure to a lesser extent) at two observation times can cause differing path delays and consequent anomalies in an InSAR deformation image. Atmospheric delay anomalies can reduce the accuracy of InSAR-derived deformation measurements from several millimetres under ideal conditions to a few centimetres under more typical conditions, thus obscuring subtle changes that could hold clues to the cause of the deformation. The difficulty with estimating water vapour conditions with the needed accuracy and spatial density is an important limiting factor in deformation monitoring with InSAR.

Four methods have been proposed to estimate the water vapour content and remove its effect from deformation interferograms. The first method is to estimate water vapour concentrations in the target area at the times of SAR image acquisitions using short-term predictions from operational weather models (Foster et al. 2006). The problem with this approach is that current weather models have much coarser resolution (a few kilometres) than InSAR measurements (tens of metres). This deficiency can be remedied to some extent by integrating weather models with high-resolution atmospheric measurements, but this approach requires intensive computation. The second method is to estimate water vapour concentration from continuous global positioning system (CGPS) observations in the target area (Li et al. 2005). The spatial resolution (i.e. station spacing) of local or regional CGPS networks at volcanoes is typically a few kilometres to tens of kilometres, which renders this method ineffective in most cases. The third approach to correcting atmospheric delay anomalies in InSAR observations is to utilize water vapour measurements from optical satellite sensors such as the Moderate Resolution Imaging Spectroradiometer (MODIS), Advanced Spaceborne Thermal Emission and Reflection Radiometer (ASTER) and European Medium Resolution Imaging Spectrometer (MERIS) (Li et al. 2003). The disadvantage of this method is the requirement of nearly simultaneous acquisitions of SAR and cloud-free optical images. The fourth and most promising technique is to correct atmospheric delay anomalies using a multitemporal InSAR technique (Section 18.6) (Ferretti et al. 2001; Lu and Dzurisin 2014). Because the atmospheric artefacts are generally spatially correlated and temporally random, they can be mitigated through temporal high-pass and spatial low-pass filtering of multitemporal interferograms.

Another significant error source in two-pass InSAR processing is baseline uncertainty due to inaccurate determination of the SAR antenna positions at the times of image acquisitions. Therefore, baseline refinement during InSAR processing is recommended. A commonly used method is to determine the baseline vector based on an existing DEM via a least-squares approach (Rosen et al. 1996). For this method, areas of the interferogram that are used to refine the baseline should have negligible deformation or deformation that is well characterized by an independent data source.

The final procedure in two-pass InSAR is to rectify the SAR images and interferograms into a geographic coordinate system, which is a backward transformation of Equation 18.5. The georeferenced interferogram (Figure 18.2h) and derived products can be readily overlaid with other data layers to enhance the utility of the interferograms and facilitate data interpretation. Figure 18.2h shows six concentric fringes that represent about 17 cm of range decrease (mostly uplift) centred on the southwest flank of Mount Peulik volcano, Alaska. The volcano inflated aseismically from October 1996 to September 1998, a period that included an intense earthquake swarm that started in May 1998 more than 30 km northwest of Peulik (Lu et al. 2002; Lu 2007; Lu and Dzurisin 2014).

Interferometric phase values need to be unwrapped to remove the modulo  $2\pi$  ambiguity before estimating the topography or deformation source parameters (Goldstein et al. 1988; Costantini 1998; Chen and Zebker 2000). Phase unwrapping is the process of restoring the correct multiple of  $2\pi$  to each pixel of the interferometric phase image. Interferograms are often spatially filtered before phase unwrapping (Goldstein and Werner 1998). Two popular phase unwrapping methods utilize branch cut (Goldstein et al. 1998) and minimum cost flow (Costantini 1998; Chen and Zebker 2000) algorithms.

In-depth descriptions of InSAR processing techniques are given by many (Zebker et al. 1994; Bamler and Hartl 1998; Henderson and Lewis 1998; Massonnet and Feigl 1998; Rosen et al. 2000; Hanssen 2001; Hensley et al. 2001; Lu and Dzurisin 2014).

## 18.5 IN SAR PRODUCTS AND THEIR APPLICATIONS TO VOLCANOES

The InSAR processing techniques include a number of steps, precise registration of an InSAR image pair, interferogram generation, removal of the curved Earth phase trend, adaptive filtering, phase unwrapping, precise estimation of the interferometric baseline, generation of a surface deformation image (or a DEM map), estimation of interferometric correlation and rectification of interferometric products. Using a single pair of SAR images as input, a typical InSAR processing chain outputs two SAR intensity images, a deformation map or DEM and an interferometric correlation map.

### 18.5.1 SAR INTENSITY IMAGE

Volcanic surfaces do not scatter microwaves uniformly. The strength of the return signal at the SAR is controlled primarily by surface roughness and relative permittivity of the target. Surface roughness refers to the SAR wavelength-scale variation in the surface relief. Surfaces that are rough at the scale of the radar wavelength generally are brighter in radar images than smooth ones, because some of the roughness elements are oriented perpendicular to the incoming signal and reflect energy back towards the source. With smooth surfaces, most of the energy is deflected forward, away from the source, which causes them to appear dark. For this reason, blocky lava flows tend to exhibit stronger backscattering returns than pyroclastic flows, which in turn produce higher backscattering than ash deposits. Therefore, SAR intensity images are useful for distinguishing and mapping volcanic ash deposits, lava flows and pyroclastic flows (Lu et al. 2004; Lu and Dzurisin 2014). In cloud-prone volcanic areas (such as the Aleutian volcanic arc), all-weather SAR intensity imagery can be one of the most useful data sources available to track the course of volcanic eruptions in this way. Relative permittivity is an electric property of material that influences radar return strength and is controlled primarily by moisture content of the imaged surface. The effect of relative permittivity variations on radar images is of secondary importance to surface roughness variations, as most

natural, dry rocks and soils have a narrow range of values of relative permittivity. Limited laboratory results have indicated that relative permittivity values of volcanic rocks of similar mineralogy and composition tend to increase with the bulk density but decrease with the porosity of volcanic rocks (Russ et al. 1999). Obviously, mapping volcanic deposits based on relative permittivity can generally be complicated by moisture content, mineralogy, composition and other parameters.

Figure 18.4 shows an example in which time-series SAR intensity images were used to track eruptive activity at Mount Cleveland volcano in the central Aleutian Arc, Alaska. Thermal anomalies at Mount Cleveland were noted in satellite data starting on 19 July 2011, and a small lava dome in the summit crater was first observed on 2 August 2011 (Lu and Dzurisin 2014). Time-series TerraSAR-X images revealed that the new dome grew rapidly until 29 December 2011, when it

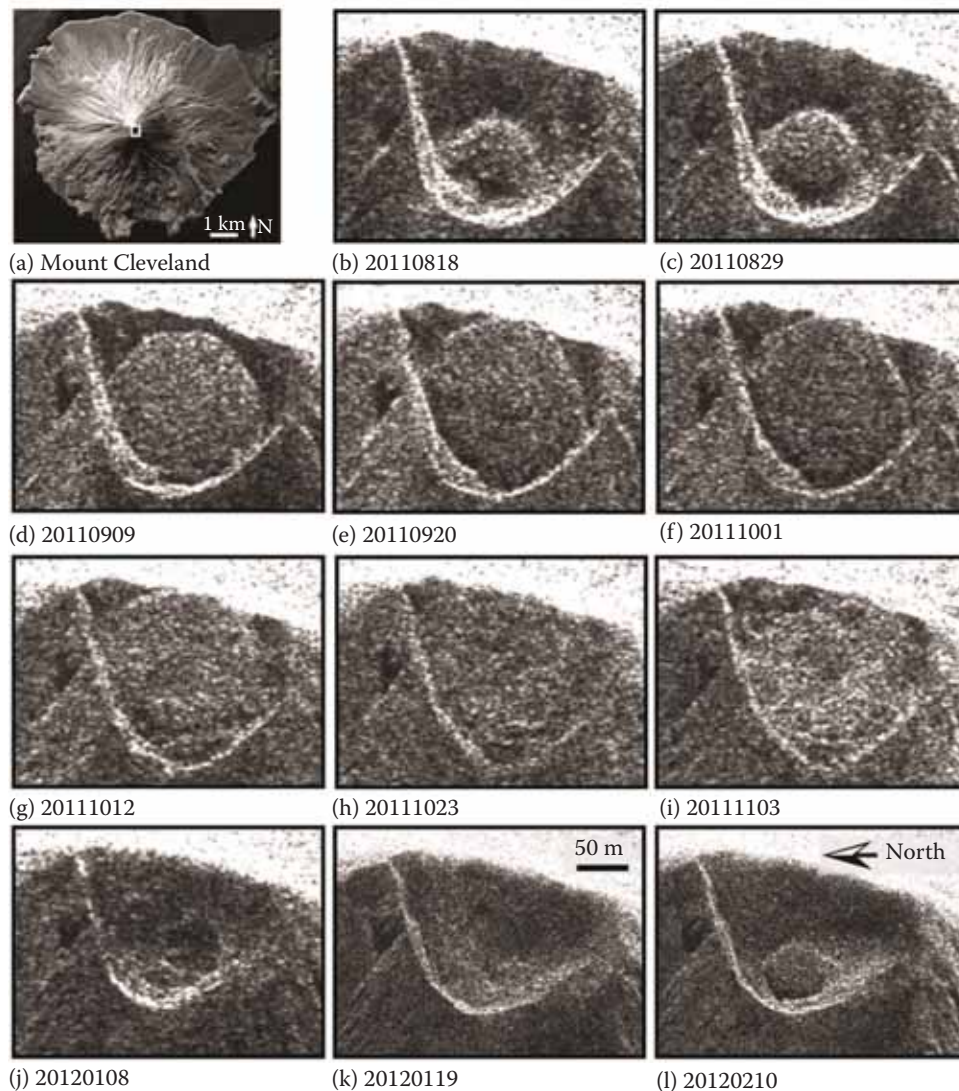


**FIGURE 18.4** (a) Airborne L-band SAR intensity image of Mount Cleveland volcano, Alaska, acquired in 2009 by NASA's Uninhabited Aerial Vehicle Synthetic Aperture Radar (UAVSAR). Lava flows of various ages are apparent in the SAR image. The white rectangle in the summit area shows the extent of the SAR intensity images shown in (b–l). (b–l) Time-series X-band TerraSAR-X intensity images of the Mount Cleveland summit crater showing lava dome growth (b–i), destruction (j–k) and regrowth (l) during the period from 18 August 2011 to 10 February 2012. The initial dome was destroyed by an explosive eruption on 29 December 2011, and a second dome was clearly visible in the SAR image acquired on 10 February 2012. Cycles of dome growth and destruction continued into 2013.

was destroyed by an explosion. A new dome was visible in a TerraSAR-X image acquired on 10 February 2012 (Figure 18.4). That dome likely was destroyed by a series of three explosions during 8–13 March 2012. A third dome, which was first seen in satellite imagery on 28 March 2012, was destroyed by an explosive eruption on 4 April 2012. Additional small explosions occurred during April–June 2012, and a fourth dome was observed in the crater on 26 June 2012. Multiple explosions were detected and a small lava flow was extruded in May 2013 (<http://avo.alaska.edu/volcanoes/volcact.php?volcname=Cleveland>). In this case, morphological changes at the summit of Mount Cleveland that could be discerned in a series of SAR intensity images, but were otherwise obscured from view, played a key role in monitoring activity throughout the course of the eruption (Wang et al. 2015).

### 18.5.2 INSAR DEFORMATION IMAGE AND SOURCE PARAMETERS DERIVED FROM MODELLING

Unlike a SAR intensity image, an InSAR deformation image is derived from phase components of two overlapping SAR images. SAR is a side-looking sensor, so an InSAR deformation image depicts ground surface displacements in the SAR line-of-sight (LOS) direction, which generally include both vertical and horizontal components. InSAR deformation images have an advantage for modelling purposes over point measurements made with GPS, for example, because InSAR images provide more complete spatial coverage than is possible with even a dense network of CGPS stations. On the other hand, CGPS stations provide better precision and much better temporal resolution than is possible with InSAR images. The temporal resolution of InSAR measurements is constrained by the orbit repeat times of SAR satellites, that is, typically several days to weeks for currently operational satellites. For hazards monitoring, a combination of periodic areal InSAR observations and continuous data streams from networks of in situ deformation sensors (e.g. CGPS, tiltmeters and strainmeters), integrated with seismic, gas emission and other remote sensing information, is highly desirable (Poland et al. 2006b; Dzurisin et al. 2009; Biggs et al. 2010b; Currenti et al. 2011, 2012; Del Negro et al. 2013).

For understanding volcanic processes, numerical models are often employed to estimate physical parameters of the deformation source based on observations. The high spatial resolution of surface deformation data provided by InSAR makes it possible to constrain models with various geometries, such as the spherical point pressure source (Mogi 1958), dislocation source (sill or dyke source) (Okada 1985), ellipsoid source (Davis 1986; Yang et al. 1988) and penny-crack source (Fialko et al. 2001). Among the physical parameters of interest, the location and volume change of the source usually are the most important.

The most widely used source in volcano deformation modelling is the spherical point pressure source (widely referred to as the Mogi source) embedded in an elastic homogeneous half space (Mogi 1958). In a Cartesian coordinate system, the predicted displacement  $u$  at the free surface due to a change in volume  $\Delta V$  or pressure  $\Delta P$  of an embedded sphere is

$$u_i(x_1 - x'_1, x_2 - x'_2, 0 - x'_3) = \Delta P(1 - \nu) \frac{r_s^3}{G} \frac{x_i - x'_i}{|R^3|} = \Delta V \frac{(1 - \nu)}{\pi} \frac{x_i - x'_i}{|R^3|} \quad (18.12)$$

where  $x'_1$ ,  $x'_2$  and  $x'_3$  are the horizontal coordinates and depth of the centre of the sphere,  $R$  is the distance between the centre of the sphere and the observation point ( $x_1$ ,  $x_2$  and 0),  $\Delta P$  and  $\Delta V$  are the pressure and volume changes in the sphere,  $\nu$  is Poisson's ratio of the host rock (typical value is 0.25),  $r_s$  is the radius of the sphere and  $G$  is the shear modulus of the host rock (Johnson 1987; Delaney and McTigue 1994).

A non-linear least-squares inversion approach is often used to optimize the source parameters (Press et al. 2007). Inverting the observed interferogram in Figure 18.2h using a Mogi source results in a best-fit source located at a depth of  $6.5 \pm 0.2$  km. The calculated volume change is

$0.043 \pm 0.002 \text{ km}^3$ . Figure 18.2i shows the modelled interferogram based on the best-fit source parameters, which agrees very well with the observed deformation field shown in Figure 18.1h.

Because many volcanic eruptions are preceded by pronounced ground deformation in response to increasing pressure in a magma reservoir or to upward intrusion of magma, surface deformation patterns can provide important insights into the structure, plumbing and state of restless volcanoes (Dvorak and Dzurisin 1997; Dzurisin 2003, 2007). Numerous studies have shown that in some cases, surface deformation is the first detectable sign of volcanic unrest, preceding seismicity or other precursors to an impending intrusion or eruption (Lu and Dzurisin 2014). Therefore, mapping surface deformation and deriving source characteristics is a primary focus of most InSAR studies of volcanoes (Massonnet et al. 1995; Lu et al. 1997, 2000a,b,c, 2002, 2005, 2007, 2010; Wicks et al. 1998, 2002, 2006, 2011; Dzurisin et al. 1999, 2005; Amelung et al. 2000, 2007; Zebker et al. 2000; Mann et al. 2002; Pritchard and Simons 2002, 2004a,b; Masterlark and Lu 2004; Fukushima et al. 2005; Lundgren and Lu 2006; Poland et al. 2006a; Wright et al. 2006; Yun et al. 2006; Hooper et al. 2007; Calais et al. 2008; Biggs et al. 2009, 2010a,b; Fournier et al. 2010; Lu and Dzurisin 2010; Ji et al. 2013; Lee et al. 2013; Parker et al. 2014).

Figure 18.5 shows several interferograms of Mount Okmok, a dominantly basaltic volcano in the central Aleutian volcanic arc, Alaska; each has a temporal separation of 1 year, and collectively they span from 1997 to 2008. Okmok erupted during February–April 1997 and again during July–August 2008. The inter-eruption deformation interferograms suggest that Okmok began to reinflate soon after its 1997 eruption, but the inflation rate generally decreased with time during 1997–2001: from about 10 cm/year during 1997–1998 to about 8 cm/year during 1998–2000, and further to about 4 cm/year during 2000–2001 (Figure 18.5b–e). The rate increased again during 2001–2003 (Figure 18.5f and g), reaching a maximum of about 20 cm/year during 2002–2003 (Figure 18.5g), before slowing to about 10 cm/year during 2003–2004 (Figure 18.5h). The caldera floor subsided 3–5 cm during 2004–2005 (Figure 18.5i), rose a similar amount during 2005–2006 (Figure 18.5j) and then did not move appreciably during 2006–2007 (Figure 18.5k). About 15 cm of uplift occurred from summer 2007 to 10 July 2008, shortly before the 12 July 2008 eruption (Figure 18.5l). This remarkable series of interferograms was interpreted as indicative of a variable rate of magma supply to a shallow storage zone beneath Okmok during the inter-eruption period of 1997–2008 (Lu et al. 2010; Lu and Dzurisin 2014).

Modelling these interferograms using a Mogi source suggests that a magma storage zone centred about ~3.5 km beneath the centre of the 10 km diameter caldera floor was responsible for the observed deformation at Okmok. The InSAR deformation images can be used to track the accumulation of magma beneath Okmok as a function of time. The total volume of magma added to the shallow storage zone from the end of the 1997 eruption to a few days before the 2008 eruption was 85%–100% of the amount that was extruded during the 1997 eruption (Lu and Dzurisin 2014).

Because InSAR is an imaging technique with good spatial resolution, it is also highly effective for mapping localized deformation associated with volcanic flows. For example, Figure 18.5k shows that the 1997 lava flow at Okmok subsided about 3 cm/year during 2006–2007, nearly a decade after it was emplaced. Lu et al. (2005) constructed two-dimensional finite element models of the localized deformation field and concluded that the subsidence likely was caused by thermoelastic cooling of the 1997 flow. They also reported that a significant amount of subsidence (1–2 cm/year) could be observed with InSAR even 50 years after emplacement of the 1958 lava flows at Okmok. This has implications for positioning geodetic markers and deformation sensors at Okmok and other similar volcanoes, and for interpretation of resulting point measurement data (e.g. GPS, tilt and borehole strain). InSAR images can provide an important spatial context for such endeavours, thus helping to avoid misinterpretations caused by unrecognized deformation sources, such as young flows, localized faulting or hydrothermal activity.

### 18.5.3 IN SAR COHERENCE IMAGE

An InSAR coherence image is a cross-correlation product derived from two co-registered complex-valued (both intensity and phase components) SAR images (Zebker and Villasenor 1992; Lu and

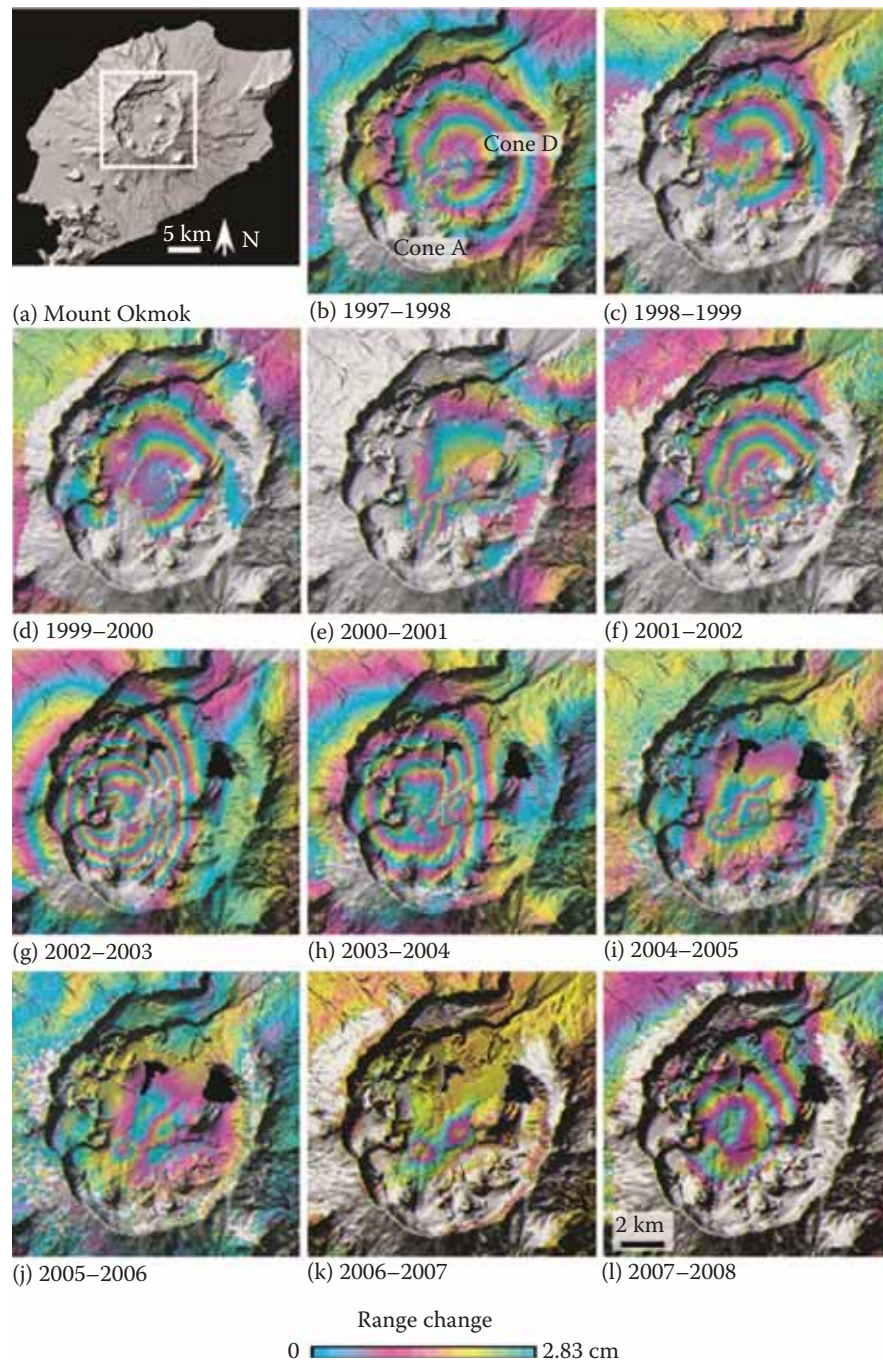


**FIGURE 18.5** (a) Shaded relief image of Mount Okmok volcano in the central Aleutian Arc, Alaska. The white square shows the extent of interferograms in (b–l). (b–l) Multitemporal 1-year InSAR images showing the intereruption deformation of Mount Okmok from 1997 (after the end of the 1997 eruption) to 2008 (before the 2008 eruption). InSAR deformation phase values are draped over the corresponding portion of the shaded relief image. Each fringe (full colour cycle) represents 2.83 cm of range change between the ground and satellite along the satellite LOS direction. Areas that lack interferometric coherence are uncoloured.

Freymueller 1998). It depicts changes in backscattering characteristics on the scale of the radar wavelength. Constructing a coherent interferogram requires that SAR images correlate with each other; that is, the backscattering spectrum must be substantially similar over the observation period. Physically, this translates into a requirement that the ground scattering surface be relatively undisturbed at the scale of the radar wavelength during the time between measurements. Loss of InSAR

coherence is often referred to as decorrelation. Decorrelation can be caused by the combined effects of (1) thermal decorrelation caused by uncorrelated noise sources in radar instruments, (2) geometric decorrelation resulting from imaging a target from very different look angles, (3) volume decorrelation caused by volume backscattering effects and (4) temporal decorrelation due to surface changes over time (Lu and Kwoun 2008).

InSAR coherence is estimated by cross-correlation of the SAR image pair within a small window of pixels. An InSAR coherence map is generated by computing the cross-correlation in a moving window over the entire image. The reliability of a deformation image or InSAR-derived DEM map can be assessed based on the InSAR coherence map. On the one hand, loss of InSAR coherence renders an InSAR image useless for measuring ground surface deformation. So for this application, the greater the coherence shown by a coherence map, the more reliable is the associated deformation image. Geometric and temporal decorrelation can be mitigated by choosing an image pair with a short baseline and brief temporal separation, respectively, so choosing such a pair is recommended when the goal is to measure surface deformation.

On the other hand, the pattern of decorrelation within a coherence image can provide useful information about surface modifications caused by volcanic activities, such as heavy ash fall or various types of flows. These phenomena modify the surface to a degree that coherence is lost, providing an efficient means to delineate the impacted areas without detailed fieldwork. Even though useful deformation measurements cannot be retrieved over areas of decorrelation, time-sequential InSAR coherence maps can be used to map the extent and progression of eruptive products, such as active lava flows. As an example, Figure 18.6 shows two TerraSAR-X InSAR coherence images along the East Rift Zone and south flank of Kīlauea volcano on the Big Island of Hawaii. The X-band images do not maintain coherence in areas of dense rainforest outside the lava flow field from the 1983 to the present Pu‘u ‘Ō‘ō–Kupaianaha eruption, nor on an active lava flow in the central part of the flow field (dark areas in the images). Elsewhere in the flow field, where young but inactive flows have cooled and stabilized, coherence is generally maintained. As a result of these differences, we can see that (1) flow activity extended all the way to the ocean during 15 September–23 December 2011, and (2) from 25 January to 25 May 2012, the flow expanded laterally but did not reach the ocean. Time-series images such as these can aid in mapping the extent and progress of volcanic flows, and thus also in assessing the inundation threat to nearby areas.

#### 18.5.4 DIGITAL ELEVATION MODEL

A precise DEM can be a very important dataset for characterizing and monitoring man-made and natural hazards, including those posed by volcanic activity. For example, a DEM is necessary to simulate potential mudflows (lahars) that are commonly associated with volcanic eruptions, large earthquakes and heavy rainfall in steep terrain. The ideal SAR configuration for DEM production is a single-pass (simultaneous) two-antenna system (e.g. SRTM). However, repeat-pass single-antenna InSAR also can be used to produce useful DEMs. Either technique is advantageous in areas where the traditional photogrammetric approach to DEM generation is hindered by persistent clouds or other factors (Lu et al. 2003; Lu and Dzurisin 2014).

There are many sources of error in DEM construction from repeat-pass SAR images, including inaccurate determination of the InSAR baseline, atmospheric delay anomalies and possible surface deformation due to tectonic, volcanic or other sources during the time interval spanned by the images. To generate a high-quality DEM, these errors must be identified and corrected using a multi-interferogram approach (Lu et al. 2003, 2013; Lu and Dzurisin 2014). A data fusion technique, such as the wavelet method, can be used to combine DEMs from several interferograms with different spatial resolution, coherence and vertical accuracy to generate the final DEM product (Ferretti et al. 1999). One example of the utility of precise InSAR-derived DEMs is illustrated in Figure 18.7, which shows the extent and thickness of a lava flow extruded during the 1997 Okmok eruption. The flow's three-dimensional distribution was derived by differencing two DEMs that represent the

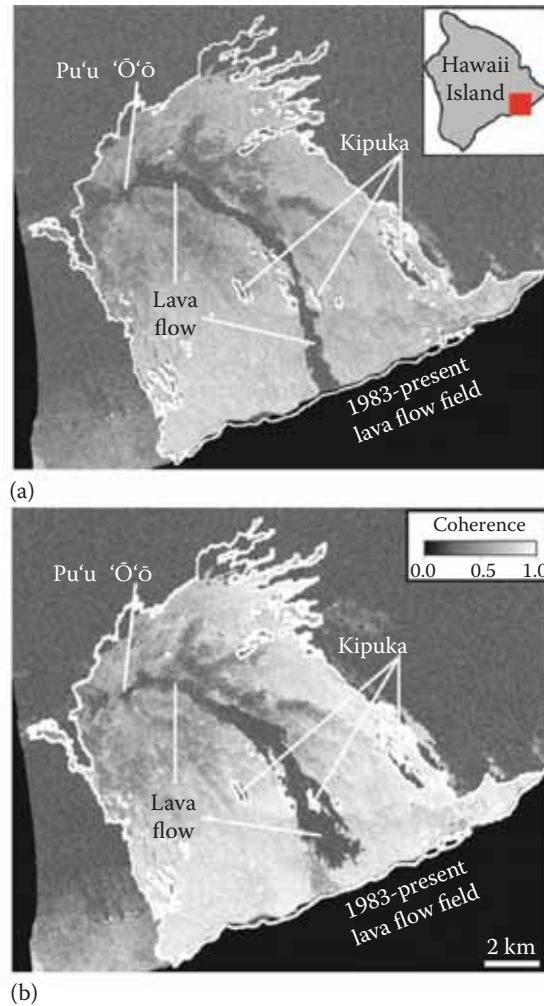


**FIGURE 18.6** TerraSAR-X InSAR coherence images showing a portion of the East Rift Zone and south flank of Kīlauea volcano, Hawaii (inset). The images span (a) 15 September–23 December 2011 and (b) 25 January–25 May 2012. The extent of lava flows from the ongoing Pu'u 'Ō'ō–Kūpaianaha eruption, which began in 1983, is outlined in white. Areas outside the lava field are covered by dense rain forest, which results in coherence loss (dark areas). The same is true for a flow in the central part of the field that was active while the images were acquired. (Images were processed and provided by Michael Poland, USGS Hawaiian Volcano Observatory.)

surface topography before and after the eruption. Multiple repeat-pass interferograms were used to correct various error sources and generate the two high-quality DEMs (Lu et al. 2003).

The TerraSAR-X tandem mission for DEM measurements (TanDEM-X) was launched by the German Aerospace Center (DLR) in 2010 (<http://www.dlr.de/hr/en/desktopdefault.aspx/tabid-2317/>). TanDEM-X is a high-resolution InSAR mission that relies on an innovative flight formation of two tandem TerraSAR-X satellites to produce InSAR-derived DEMs on a global scale with accuracy better than that of SRTM (Krieger et al. 2007). X-band SARs on the two satellites record data synchronously with a closely controlled baseline separation of 200–500 m. Precise baseline information and simultaneous data acquisitions result in InSAR images that are nearly immune to the baseline errors, atmospheric contamination and temporal decorrelation that sometimes plague DEMs derived from repeat-pass InSAR. Thus, the TanDEM-X mission enables the production of a global DEM of unprecedented accuracy, coverage and quality: TanDEM-X DEMs have a specified relative vertical accuracy of 2 m and an absolute vertical accuracy of 10 m at a horizontal resolution of 12 m (Krieger et al. 2007).

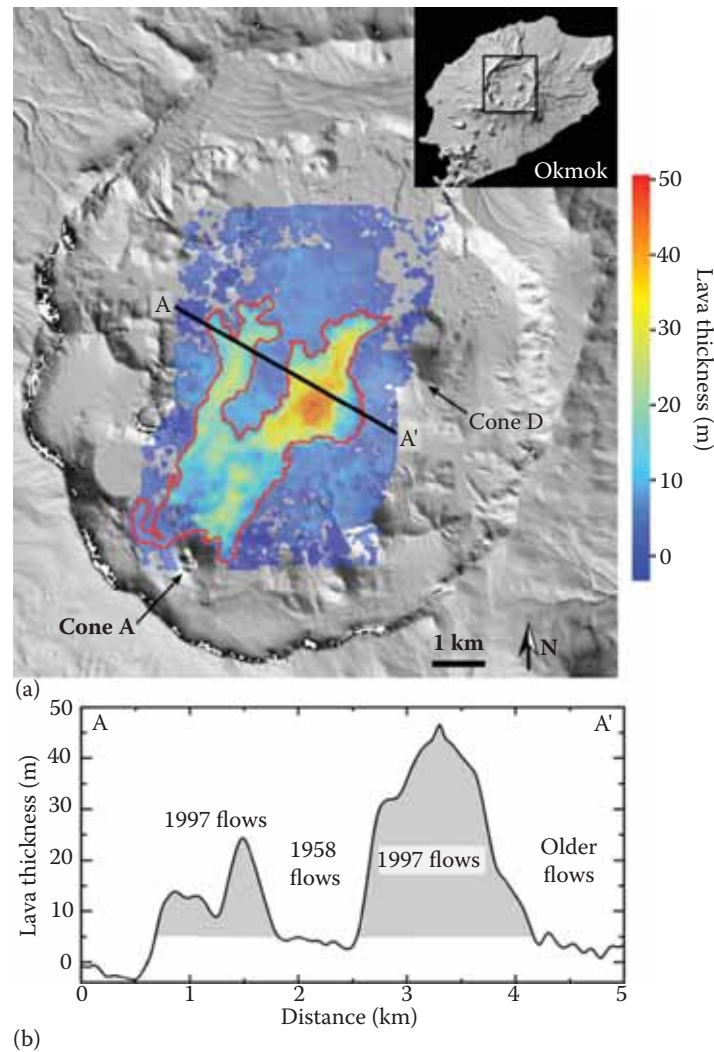


**FIGURE 18.7** Thickness of lava flows from the 1997 eruption at Mount Okmok produced by differencing pre- and post-eruption DEMs derived from InSAR. (a) Map view of the 1997 lava flows. The red line represents the flow perimeter based on field mapping in August 2001 (Lu et al. 2003). The inset is a shaded relief image of Okmok; the black rectangle shows the extent of (a). (b) Lava thickness along the profile A-A' across the 1997 flows and a small portion of the underlying 1958 flows that are not covered by 1997 flows. The locations of A-A' are shown in (a).

## 18.6 MULTI-INTERFEROGRAM InSAR

When more than two SAR images are available for a given study area, multi-interferogram InSAR processing can be employed to improve the accuracy of deformation maps (or other InSAR products) (Ferretti et al. 2001, 2007; Berardino et al. 2002; Hooper et al. 2007; Rocca 2007; Zhang et al. 2011, 2012; Lu and Dzurisin 2014; Lu and Zhang 2014). A goal of multi-interferogram InSAR processing is to characterize the spatial and temporal behaviours of the deformation signal plus various artefacts and noise sources (e.g. atmospheric delay anomalies, including radar frequency-dependent ionosphere refraction and non-dispersive troposphere delay of the radar signals; orbit errors; and DEM-induced artefacts) in individual interferograms, and then to remove the artefacts to retrieve time-series deformation measurements at the SAR pixel level.

Among several approaches to multi-interferogram analysis, persistent scatterer InSAR (PSInSAR) is one of the newest and most promising. PSInSAR exploits the distinctive backscattering characteristics of certain ground targets (PS; examples include buildings, houses, bridges, dams,

large boulders or rock outcrops) and the unique characteristics of atmospheric delay anomalies to improve the accuracy of conventional InSAR deformation measurements (Ferretti et al. 2001). The SAR backscattering signal of a PS target has a broadband spectrum in the frequency domain, which implies that the radar phase of a PS target correlates over much longer time intervals and over much longer baselines than that of other targets. As a result, if the backscatter signal from a given pixel is dominated by return from one or more PSs, the pixel remains coherent over longer time intervals and longer baselines than it would in the absence of the PS pixels. Therefore, at PS pixels, the limitation imposed by loss of coherence in conventional InSAR analysis can be overcome. Because InSAR coherence is maintained at PS pixels, the atmospheric contribution to the

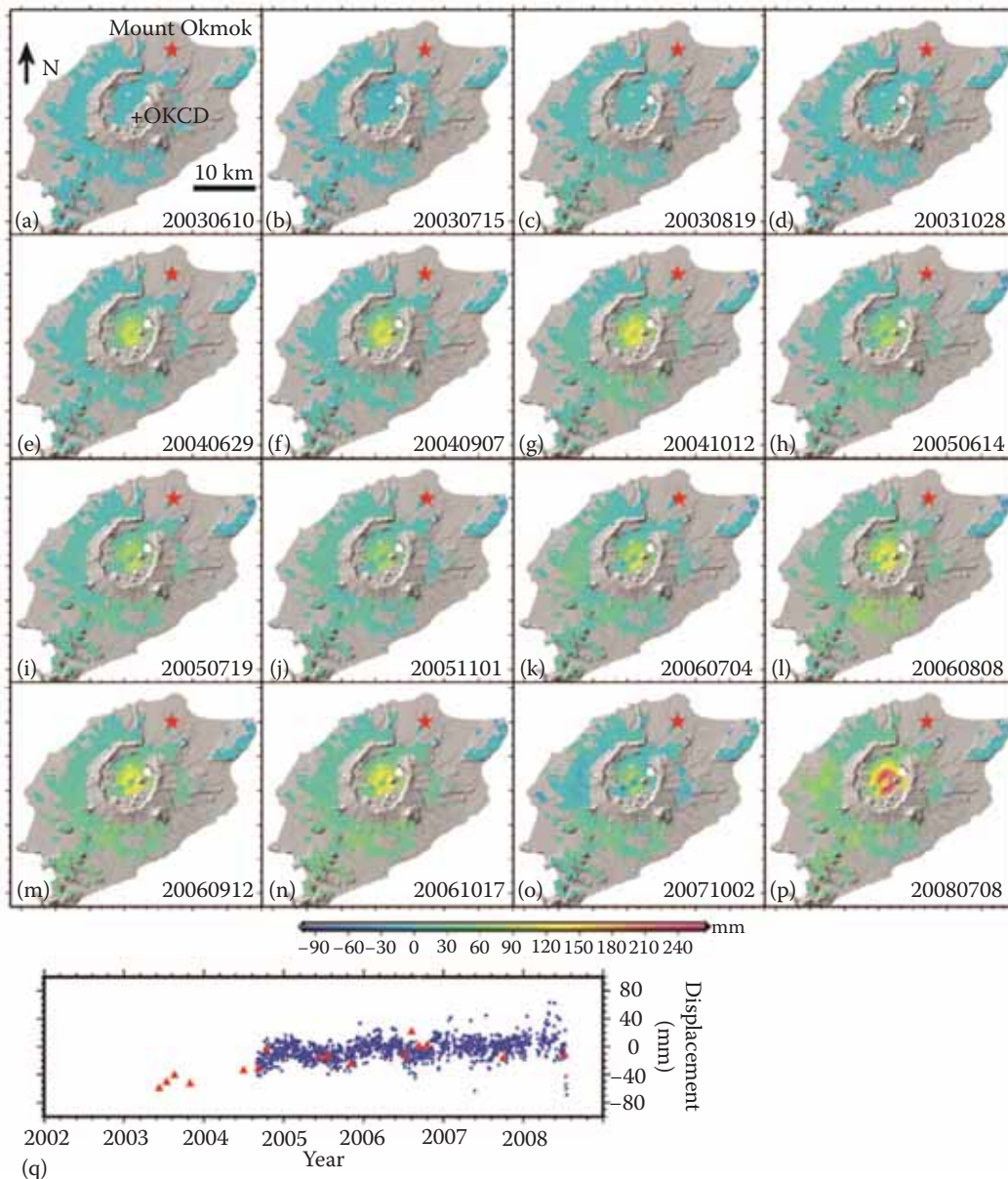


**FIGURE 18.8** (a–p) Time-series deformation maps for Mount Okmok based on PSInSAR processing of 19 Envisat SAR images acquired during 2003–2008. The red star in the northeast quadrant represents the pixel used for PSInSAR processing. The location of the CGPS station OKCD is indicated by a black cross (+) in (a). (q) Comparison of time-series PSInSAR measurements (red triangles) with CGPS observations (blue dots) at OKCD. PSInSAR displacements are with respect to the reference pixel; the start time of the PSInSAR time series is 10 June 2003.

backscattered signal, DEM error and orbit error can be identified and removed from the data using a multi-interferogram iterative approach. After these errors are removed, displacement histories at PS pixels can be resolved with millimetre accuracy. If a sufficient number of PS pixels exist in a series of interferograms, relative displacements among them can provide a detailed picture of the surface deformation field.

Figure 18.8a–p shows time-series deformation maps for the period 2003–2008 at Mount Okmok based on PSInSAR processing of a stack of 19 Envisat SAR images. The average inflation rate near the centre of the caldera is slightly less than 50 mm/year. The subsidence of 1997 lava flows on parts of the caldera floor is also discernible in some of the images. The PSInSAR-derived time-series displacements match CGPS measurements at nearby points (Figure 18.8q), demonstrating that PSInSAR can be useful either as a stand-alone tool or in conjunction with other techniques to track volcanic deformation.

## 18.7 CONCLUSION

Radar in various forms can provide timely observations of volcanic ash clouds, eruptive flows and ground surface deformation before, during and after eruptions. SAR and InSAR products can be used to (1) characterize changing volcanic landscapes that might otherwise be unmonitored or hidden from view, (2) map and measure the deformation of volcanic flows that can persist for decades, (3) estimate physical parameters of subsurface magma reservoirs and conduit systems, (4) monitor changes in reservoir volume and magma migration pathways and (5) contribute to eruption forecasts and volcanic hazard assessments. With more satellite radar platforms either operational or in the planning stages, SAR and InSAR are becoming increasingly important tools for studying volcanoes and associated hazards.

## ACKNOWLEDGEMENTS

ERS-1, ERS-2 and Envisat, and TerraSAR-X SAR images are Copyright © 1992–2011 European Space Agency and © 2011–2012 DLR, respectively. ERS-1 and ERS-2 SAR images were provided by Alaska Satellite Facility. We thank Lei Zhang, Michael Poland, and David Schneider and Richard Hoblitt for providing the materials used in Figures 18.8, 18.6 and 18.1, respectively. This work was supported by the National Aeronautics and Space Administration's (NASA) Earth Surface and Interior Program (NNX14AQ95G), the U.S. Geological Survey (USGS) Volcano Hazards Program and the Shuler–Foscue Endowment at Southern Methodist University.

## REFERENCES

- Amelung, F., Jonsson, S., Zebker, H., and Segall, P. (2000). Widespread uplift and 'trapdoor' faulting on Galapagos volcanoes observed with radar interferometry. *Nature*, 407, 993–996.
- Amelung, F., Yun, S. H., Walter, T. R., Segall, P., and Kim, S. W. (2007). Stress control of deep rift intrusion at Mauna Loa volcano, Hawaii. *Science*, 316, 1026–1030.
- Bamler, R., and Hart, P. (1998). Synthetic aperture radar interferometry. *Inverse Problems*, 14, R1–R54.
- Berardino, P., Fornaro, G., Lanari, R., and Sansosti, E. (2002). A new algorithm for surface deformation monitoring based on small baseline differential SAR interferograms. *IEEE Transactions on Geoscience and Remote Sensing*, 40, 2375–2383.
- Biggs, J., Amelung, F., Gourmelen, N., Dixon, T., and Kim, S. W. (2009). InSAR observations of 2007 Tanzania rifting episode reveal mixed fault and dyke extension in an immature continental rift. *Geophysical Journal International*, 179, 549–558.
- Biggs, J., Anthony, E. Y., and Ebinger, C. J. (2010a). Multiple inflation and deflation events at Kenyan volcanoes, East African Rift. *Geology*, 37, 979–982.
- Biggs, J., Lu, Z., Fournier, T., and Freymueller, J. (2010b). Magma flux at Okmok Volcano, Alaska from a joint inversion of continuous GPS, campaign GPS and InSAR. *Journal of Geophysical Research*, 115, B12401. doi: 10.1029/2010JB007577.

- Calais, E., d'Oreye, N., Albaric, J., Deschamps, A., Delvaux, D., Déverchère, J., Ebinger, C. et al. (2008). Aseismic strain accommodation by dyking in a youthful continental rift, East Africa. *Nature*, 456, 783–787. doi: 10.1038/nature07478.
- Chen, C., and Zebker, H. (2000). Network approaches to two-dimensional phase unwrapping: Intractability and two new algorithms. *Journal of the Optical Society of America A*, 17, 401–414.
- Costantini, M. (1998). A novel phase unwrapping method based on network programming. *IEEE Transactions on Geoscience and Remote Sensing*, 36, 813–818.
- Curlander, J. C., and McDonough, R. N. (1991). *Synthetic Aperture Radar: Systems and Signal Processing*. 1st ed., Wiley Series in Remote Sensing and Image Processing. Hoboken, NJ: Wiley-Interscience.
- Currenti, G., Napoli, R., and Del Negro, C. (2011). Toward a realistic deformation model of the 2008 magmatic intrusion at Etna from combined DInSAR and GPS observations. *Earth and Planetary Science Letters*, 312, 22–27.
- Currenti, G., Solaro, G., Napoli, R., Pepe, A., Bonaccorso, A., Del Negro, C., and Sansosti, E. (2012). Modelling of ALOS and COSMO-SkyMed satellite data at Mt Etna: Implications on relation between seismic activation of the Pernicana fault system and volcanic unrest. *Remote Sensing of Environment*, 125, 64–72.
- Davis, P. M. (1986). Surface deformation due to inflation of an arbitrarily oriented triaxial ellipsoidal cavity in an elastic half-space, with reference to Kīlauea Volcano, Hawaii. *Journal of Geophysical Research*, 91, 7429–7438.
- Delaney, P. T., and McTigue, D. F. (1994). Volume of magma accumulation or withdrawal estimated from surface uplift or subsidence, with application to the 1960 collapse of Kīlauea volcano. *Bulletin of Volcanology*, 56, 417–424.
- Del Negro, C., Currenti, G., Solaro, G., Greco, F., Pepe, A., Napoli, R., Pepe, S., Casu, F., and Sansosti, E. (2013). Capturing the fingerprint of Etna volcano activity in gravity and satellite radar data. *Scientific Reports*, 3, 3089. doi: 10.1038/srep03089.
- Duboscclard, G., Cordesses, R., Alard, P., Hervier, C., Coltelli, M., and Kornprobst, J. (1999). First testing of a volcano Doppler radar (Voldorad) at Mt. Etna. *Journal of Geophysical Research*, 26, 3389–3392.
- Dvorak, J., and Dzurisin, D. (1997). Volcano geodesy—The search for magma reservoirs and the formation of eruptive vents. *Reviews of Geophysics*, 35, 343–384.
- Dzurisin, D. (2003). A comprehensive approach to monitoring volcano deformation as a window on eruption cycle. *Reviews of Geophysics*, 41, 1–29. doi: 10.1029/2001RG000107.
- Dzurisin, D. (2007). *Volcano Deformation—Geodetic Monitoring Techniques*. Vol. 7, Springer-Praxis Books in Geophysical Sciences. Berlin: Springer.
- Dzurisin, D., Lisowski, M., and Wicks, C. W. (2009). Continuing inflation at Three Sisters volcanic center, central Oregon Cascade Range, USA, from GPS, leveling, and InSAR observations. *Bulletin of Volcanology*, 71, 1091–1110.
- Dzurisin, D., Lisowski, M., Wicks, C. W., Poland, M. P., and Endo, E. T. (2005). Geodetic observations and modeling of magmatic inflation at the Three Sisters volcanic center, central Oregon Cascade Range, USA. *Journal of Volcanology and Geothermal Research*, 150, 35–54.
- Dzurisin, D., Wicks, C., Jr., and Thatcher, W. (1999). Renewed uplift at the Yellowstone caldera measured by leveling surveys and satellite radar interferometry. *Bulletin of Volcanology*, 61, 349–355.
- Farr, T. G., Rosen, P. A., Caro, E., Crippen, R., Duren, R., Hensley, S., Kobrick, M. et al. (2007). The Shuttle Radar Topography Mission. *Reviews of Geophysics*, 45, RG2004. doi: 10.1029/2005RG000183.
- Ferretti, A., Prati, C., and Rocca, F. (1999). Multibaseline InSAR DEM reconstruction—The wavelet approach. *IEEE Transactions on Geoscience and Remote Sensing*, 37, 705–715.
- Ferretti, A., Prati, C., and Rocca, F. (2001). Permanent scatterers in SAR interferometry. *IEEE Transactions on Geoscience and Remote Sensing*, 39, 8–20.
- Ferretti, A., Savio, G., Barzaghi, R., Borghi, A., Musazzi, S., Novali, F., Prati, C., and Rocca, F. (2007). Submillimeter accuracy of InSAR time series: Experimental validation. *IEEE Transactions on Geoscience and Remote Sensing*, 45, 1142–1153.
- Fialko, Y., Khazan, Y., and Simons, M. (2001). Deformation due to a pressurized horizontal circular crack in an elastic half-space, with applications to volcano geodesy. *Geophysical Journal International*, 146, 181–190.
- Foster, J., Brooks, B., Cherubini, T., Shacat, C., Businger, S., and Werner, C. L. (2006). Mitigating atmospheric noise for InSAR using a high resolution weather model. *Geophysical Research Letters*, 33, L16304. doi: 10.1029/2006GL026781.
- Fournier, T. J., Pritchard, M. E., and Riddick, S. N. (2010). Duration, magnitude, and frequency of subaerial volcano deformation events: New results from Latin America using InSAR and a global synthesis. *Geochemistry, Geophysics, Geosystems*, 11, Q01003. doi: 10.1029/2009GC002558.

- Fukushima, Y., Cayol, V., and Durand, P. (2005). Finding realistic disk models from interferometric synthetic aperture radar data: The February 2000 eruption at Piton de la Fournaise. *Journal of Geophysical Research*, 110, B03206. doi: 10.1029/2004JG0003268.
- Gray, L., and Farris-Manning, P. (1993). Repeat-pass interferometry with airborne synthetic aperture radar. *IEEE Transactions on Geoscience and Remote Sensing*, 31, 180–191.
- Goldstein, R., Zebker, H., and Werner, C. (1998). Satellite radar interferometry: Two-dimensional phase unwrapping. *Radio Science*, 23, 713–720.
- Goldstein, R. M., and Werner, C. L. (1998). Radar interferogram filtering for geophysical applications. *Geophysical Research Letters*, 25, 4035–4038.
- Hanssen, R. (2001). *Radar Interferometry—Data Interpretation and Error Analysis*. Dordrecht, the Netherlands: Kluwer Academic Publishers.
- Harris, D. M., and Rose, W. I. (1983). Estimating particle sizes, concentrations and total mass of ash in volcanic clouds using weather radar. *Journal of Geophysical Research*, 88, 10969–10983.
- Henderson, F., and Lewis, A. (1998). *Principles and Applications of Imaging Radar: Manual of Remote Sensing*. 3rd ed., vol. 2. Hoboken, NJ: John Wiley & Sons.
- Hensley, S., Munjy, R., and Rosen, P. (2001). Interferometric synthetic aperture radar (IFSAR). In *Digital Elevation Model Technologies and Applications—The DEM Users Manual*, ed. D. F. Maune. 2nd ed. Bethesda, MD: American Society for Photogrammetry and Remote Sensing, 142–206.
- Hildreth, W., and Fierstein, J. (2012). The Novarupta-Katmai eruption of 1912—Largest eruption of the twentieth century; centennial perspectives. U.S. Geological Survey Professional Paper 1791. <http://pubs.usgs.gov/pp/1791/>.
- Hooper, A., Segall, P., and Zebker, H. (2007). Persistent scatterer interferometric synthetic aperture radar for crustal deformation analysis, with application to Volcán Alcedo, Galápagos. *Journal of Geophysical Research*, 112, B07407. doi: 10.1029/2006JB004763.
- Houlié, N., Briole, P., Necessian, A., and Murakami, M. (2005). Sounding the plume of the 18 August 2000 eruption of Miyakejima volcano (Japan) using GPS. *Geophysical Research Letters*, 32, L05302.
- Ji, L. Y., Lu, Z., Dzurisin, D., and Senyukov, S. (2013). Pre-eruption deformation caused by dike intrusion beneath Kizimen volcano, Kamchatka, Russia, observed by InSAR. *Journal of Volcanology and Geothermal Research*, 256, 87–95.
- Johnson, D. J. (1987). Elastic and inelastic magma storage at Kīlauea volcano. In *Volcanism in Hawaii*, ed. R. W. Decker, T. L. Wright, and P. H. Stauffer. U.S. Geological Survey Professional Paper 1350. Washington, DC: U.S. Government Printing Office, 1297–1306.
- Krieger, G., Moreira, A., Fiedler, H., Hajnsek, I., Werner, M., Younis, M., and Zink, M. (2007). TanDEM-X—A satellite formation for high-resolution SAR interferometry. *IEEE Transactions on Geoscience and Remote Sensing*, 45, 3317–3341.
- Lacasse, C., Karlsdóttir, S., Larsen, G., Soosalu, H., Rose, W. I., and Ernst, G. G. J. (2004). Weather radar observations of the Hekla 2000 eruption cloud, Iceland. *Bulletin of Volcanology*, 66, 457–473.
- Lee, C. W., Lu, Z., Won, J. S., Jung, H. S., and Dzurisin, D. (2013). Dynamic deformation of Seguam Island, Alaska, 1992–2008, from multi-interferogram InSAR processing. *Journal of Volcanology and Geothermal Research*, 260, 43–51.
- Li, Z., Fielding, E., Cross, P., and Muller, J.-P. (2005). InSAR atmospheric correction—GPS topography-dependent turbulence model (GTTM). *Journal of Geophysical Research*, 110, B02404. doi: 10.1029/2005JB003711.
- Li, Z., Muller, J.-P., and Cross, P. (2003). Comparison of precipitable water vapor derived from radiosonde, GPS, and moderate-resolution imaging spectroradiometer measurements. *Journal of Geophysical Research*, 108, 4651. doi: 10.1029/2003JD003372.
- Lu, Z. (2007). InSAR imaging of volcanic deformation over cloud-prone areas—Aleutian Islands. *Photogrammetric Engineering & Remote Sensing*, 73, 245–257.
- Lu, Z., and Dzurisin, D. (2010). Ground surface deformation patterns, magma supply, and magma storage at Okmok volcano, Alaska, inferred from InSAR analysis: II. Co-eruptive deflation, July–August 2008. *Journal of Geophysical Research*, 115, B00B02. doi: 10.1029/2009JB006970.
- Lu, Z., and Dzurisin, D. (2014). *InSAR Imaging of Aleutian Volcanoes—Monitoring a Volcanic Arc from Space*. Springer-Praxis Books in Geophysical Sciences. Berlin: Springer.
- Lu, Z., Dzurisin, D., Biggs, J., Wicks, C., Jr., and McNutt, S. (2010). Ground surface deformation patterns, magma supply, and magma storage at Okmok volcano, Alaska, from InSAR analysis: I. Inter-eruption deformation, 1997–2008. *Journal of Geophysical Research*, 115, B00B03. doi: 10.1029/2009JB006969.

- Lu, Z., Dzurisin, D., Wicks, C., Power, J., Kwoun, O., and Rykhus, R. (2007). Diverse deformation patterns of Aleutian volcanoes from satellite interferometric synthetic aperture radar (InSAR). In *Volcanism and Subduction: The Kamchatka Region*, ed. J. Eichelberger, E. Gordeev, P. Izbekov, M. Kasahara, and J. Lees. American Geophysical Union Geophysical Monograph Series 172. Washington, DC: American Geophysical Union, 249–261.
- Lu, Z., Fatland, R., Wyss, M., Li, S., Eichelberger, J., Dean, K., and Freymueller, J. T. (1997). Deformation of volcanic vents detected by ERS 1 SAR interferometry, Katmai National Park, Alaska. *Geophysical Research Letters*, 24, 695–698.
- Lu, Z., and Freymueller, J. (1998). Synthetic aperture radar interferometry coherence analysis over Katmai volcano group, Alaska. *Journal of Geophysical Research*, 103, 29887–29894.
- Lu, Z., Fielding, E., Patrick, M., and Trautwein, C. (2003). Estimating lava volume by precision combination of multiple baseline spaceborne and airborne interferometric synthetic aperture radar: The 1997 eruption of Okmok volcano, Alaska. *IEEE Transactions on Geoscience and Remote Sensing*, 41, 1428–1436.
- Lu, Z., Jung, H. S., Zhang, L., Lee, W. J., Lee, C. W., and Dzurisin, D. (2013). DEM generation from satellite InSAR. In *Advances in Mapping from Aerospace Imagery: Techniques and Applications*, ed. X. Yang and J. Li. Boca Raton, FL: CRC Press, 119–144.
- Lu, Z., Mann, D., Freymueller, J., and Meyer, D. (2000c). Synthetic aperture radar interferometry of Okmok volcano, Alaska: Radar observations. *Journal of Geophysical Research*, 105, 10791–10806.
- Lu, Z., Masterlark, T., and Dzurisin, D. (2005). Interferometric synthetic aperture radar (InSAR) study of Okmok volcano, Alaska, 1992–2003: Magma supply dynamics and post-emplacement lava flow deformation. *Journal of Geophysical Research*, 110, B02403. doi: 10.1029/2004JB003148.
- Lu, Z., and Kwoun, O. (2008). Radarsat-1 and ERS interferometric analysis over southeastern coastal Louisiana: Implication for mapping water-level changes beneath swamp forests. *IEEE Transactions on Geoscience and Remote Sensing*, 46, 2167–2184.
- Lu, Z., Power, J., McConnell, V., Wicks, C., and Dzurisin, D. (2002). Pre-eruptive inflation and surface interferometric coherence characteristics revealed by satellite radar interferometry at Makushin volcano, Alaska: 1993–2000. *Journal of Geophysical Research*, 107, 2266. doi: 10.1029/2001JB000970.
- Lu, Z., Rykhus, R., Masterlark, T., and Dean, K. (2004). Mapping recent lava flows at Westdahl volcano, Alaska, using radar and optical satellite imagery. *Remote Sensing of Environment*, 91, 345–353.
- Lu, Z., Wicks, C., Dzurisin, D., Power, J., Moran, S., and Thatcher, W. (2002). Magmatic inflation at a dormant stratovolcano—1996–98 activity at Mount Peulik volcano, Alaska, revealed by satellite radar interferometry. *Journal of Geophysical Research*, 107, 2134. doi: 10.1029/2001JB000471.
- Lu, Z., Wicks, C., Dzurisin, D., Thatcher, W., Freymueller, J., McNutt, S., and Mann, D. (2000b). Aseismic inflation of Westdahl volcano, Alaska, revealed by satellite radar interferometry. *Geophysical Research Letters*, 27, 1567–1570.
- Lu, Z., Wicks, C., Power, J., and Dzurisin, D. (2000a). Ground deformation associated with the March 1996 earthquake swarm at Akutan volcano, Alaska, revealed by satellite radar interferometry. *Journal of Geophysical Research*, 105, 21483–21496.
- Lu, Z., and Zhang, L. (2014). Frontiers of Radar Remote Sensing. *Photogrammetric Engineering & Remote Sensing*, 80, 5–13.
- Lundgren, P., and Lu, Z. (2006). Inflation model of Uzon caldera, Kamchatka, constrained by satellite radar interferometry observations. *Geophysical Research Letters*, 33, L063012. doi: 10.1029/2005GL025181.
- Mann, D., Freymueller, J., and Lu, Z. (2002). Deformation associated with the 1997 eruption of Okmok volcano, Alaska. *Journal of Geophysical Research*, 107, 10.1029/2001JB000163.
- Marzano, F. S., Barbieri, S., Vulpiani, G., and Rose, W. I. (2006). Volcanic ash cloud retrieval by ground-based microwave weather radar. *IEEE Transactions on Geoscience and Remote Sensing*, 44, 3235–3246.
- Massonnet, D., Briole, P., and Arnaud, A. (1995). Deflation of Mount Etna monitored by spaceborne radar interferometry. *Nature*, 375, 567–570.
- Massonnet, D., and Feigl, K. (1998). Radar interferometry and its application to changes in the earth's surface. *Reviews of Geophysics*, 36, 441–500.
- Massonnet, D., and Souyris, J. S. (2008). *Imaging with Synthetic Aperture Radar*. Lausanne, Switzerland: EPFL Press.
- Masterlark, T., and Lu, Z. (2004). Transient volcano deformation sources imaged with InSAR: Application to Seguam island. *Journal of Geophysical Research*, 109, B01401. doi: 10.1029/2003JB002568.
- Miller, T. P., and Casadevall, T. J. (2000). Volcanic ash hazards to aviation. In *Encyclopaedia of Volcanology*, ed. H. Sigurdsson. New York: Academic, 915–930.
- Mogi, K. (1958). Relations between the eruptions of various volcanoes and the deformation of the ground surfaces around them. *Bulletin of the Earthquake Research Institute, University of Tokyo*, 36, 99–134.

- Myers, B., Brantley, S. R., Stauffer, P., and Hendley, J. W., II. (2008). What are volcano hazards? USGS Fact Sheet 002-97. <http://pubs.usgs.gov/fs/fs002-97/>.
- Newhall, C. G., and Punongbayan, R. S. (1996). Eruptive history of Mount Pinatubo. In *Fire and Mud: Eruptions and Lahars of Mount Pinatubo, Philippines*. Seattle: University of Washington Press, 165–195.
- Okada, Y. (1985). Surface deformation due to shear and tensile faults in a half-space. *Bulletin of the Seismological Society of America*, 75, 1135–1154.
- Parker, A., Biggs, J., and Lu, Z. (2014). Investigating long-term subsidence at Medicine Lake Volcano, CA, using multi-temporal InSAR. *Geophysical Journal International*, 199, 844–859.
- Poland, M. P., Bürgmann, R., Dzurisin, D., Lisowski, M., Masterlark, T., Owen, S., and Fink, J. (2006a). Constraints on the mechanism of long-term, steady subsidence at Medicine Lake volcano, northern California, from GPS, leveling, and InSAR. *Journal of Volcanology and Geothermal Research*, 150, 55–78.
- Poland, M., Hamburger, M., and Newman, A. (2006b). The changing shapes of active volcanoes: History, evolution, and future changes for volcano geodesy. *Journal of Volcanology and Geothermal Research*, 150, 1–13. doi: 10.1016/j.jvolgeores.2005.11.005.
- Press, W. H., Teukolsky, S. A., Vetterling, W. T., and Flannery, B. P. (2007). *Numerical Recipes in C—The Art of Scientific Computing*. 3rd ed. Cambridge: Cambridge University Press.
- Pritchard, M. E., and Simons, M. (2002). A satellite geodetic survey of large-scale deformation of volcanic centres in the central Andes. *Nature*, 418, 167–171.
- Pritchard, M. E., and Simons, M. (2004a). An InSAR-based survey of volcanic deformation in the central Andes. *Geochemistry, Geophysics, Geosystems*, 5. doi: 10.1029/2003GC000610.
- Pritchard, M. E., and Simons, M. (2004b). Surveying volcanic arcs with satellite radar interferometry: The central Andes, Kamchatka, and beyond. *GSA Today*, 14, 4–11.
- Robock, A. (2013). The latest on volcanic eruptions and climate. *Eos, Transactions, American Geophysical Union*, 94, 305–312.
- Rocca, F. (2007). Modeling interferogram stacks. *IEEE Transactions on Geoscience and Remote Sensing*, 45, 3289–3299.
- Rose, W. I. (1977). Scavenging of volcanic aerosol by ash: Atmospheric and volcanological implications. *Geology*, 5, 621–624.
- Rose, W. I., Kostinski, A. B., and Kelley, L. (1995). Real time C band radar observations of 1992 eruption clouds from Crater Peak/Spurr volcano, Alaska. *U.S. Geological Survey Bulletin*, 2139, 19–26.
- Rosen, P., Hensley, S., Joughin, I. R., Li, F. K., Madsen, S. N., Rodriguez, E., and Goldstein, R. M. (2000). Synthetic aperture radar interferometry. *Proceedings of the IEEE*, 88, 333–380.
- Rosen, P., Hensley, S., Zebker, H., Webb, F. H., and Fielding, E. J. (1996). Surface deformation and coherence measurements of Kīlauea volcano, Hawaii, from SIR-C radar interferometry. *Journal of Geophysical Research*, 101, 23109–23125.
- Rust, A. C., Russell, J. K., and Knight, R. J. (1999). Dielectric constant as a predictor of porosity in dry volcanic rocks. *Journal of Volcanology and Geothermal Research*, 91, 79–96.
- Schneider, D., and Hoblitt, R. (2013). Doppler weather radar observations of the 2009 eruption of Redoubt volcano, Alaska. *Journal of Volcanology and Geothermal Research*, 259, 133–144.
- Tupper, A., Oswalt, J. S., and Rosenfield, D. (2005). Satellite and radar analysis of volcanic-cumulonimbus at Mount Pinatubo, Philippines, 1991. *Journal of Geophysical Research*, 110, D9204, <http://dx.doi.org/10.1029/2004JD005499>.
- Wang, T., Poland, M. P., and Lu, Z. (2015). Dome growth at Mount Cleveland, Aleutian Arc, quantified by time series TerraSAR-X imagery. *Geophysical Research Letters*, 42, 1–8. doi: 10.1002/2015GL066784.
- Wicks, C., de la Llera, J. C., Lara, L., and Lowenstern, J. (2011). The role of dyking and fault control in the rapid onset of eruption at Chaitén volcano, Chile. *Nature*, 478, 374–377.
- Wicks, C., Dzurisin, D., Ingebritsen, S., Thatcher, W., Lu, Z., and Iverson, J. (2002). Magma intrusion beneath the Three Sisters Volcanic Center in the Cascade Range of Oregon, USA, from interferometric radar measurements. *Geophysical Research Letters*, 29. doi: 10.1029/2001GL014205.
- Wicks, C., Thatcher, W., and Dzurisin, D. (1998). Migration of fluids beneath Yellowstone caldera inferred from satellite radar interferometry. *Science*, 282, 458–462.
- Wicks, C., Thatcher, W., Dzurisin, D., and Svarc, J. (2006). Uplift, thermal unrest and magma intrusion at Yellowstone caldera. *Nature*, 440, 72–75.
- Wright, T., Ebinger, C., Biggs, J., Ayele, A., Yirgu, G., Keir, D., and Stork, A. (2006). Magma-maintained rift segmentation at continental rupture in the 2005 Afar dyking episode. *Nature*, 442, 291–294.
- Yang, X.-M., Davis, P. M., and Dieterich, J. H. (1988). Deformation from inflation of a dipping finite prolate spheroid in an elastic half-space as a model for volcanic stressing. *Journal of Geophysical Research*, 93, 4249–4257.

- Yun, S., Segall, P., and Zebker, H. (2006). Constraints on magma chamber geometry at Sierra Negra Volcano, Galapagos Islands, based on InSAR observations. *Journal of Volcanology and Geothermal Research*, 150, 232–243.
- Zebker, H., Amelung, F., and Jonsson, S. (2000). Remote sensing of volcano surface and internal processing using radar interferometry. In *Remote Sensing of Active Volcanism*, ed. P. Mouginiis-Mark, J. A. Crisp, and J. H. Fink. AGU Monograph. Washington, DC: American Geophysical Union, 179–205.
- Zebker, H. A., Rosen, P. A., Goldstein, R. M., Gabriel, A., and Werner, C. L. (1994). On the derivation of coseismic displacement fields using differential radar interferometry—The Landers earthquake. *Journal of Geophysical Research*, 99, 19617–19634.
- Zebker, H., and Villasenor, J. (1992). Decorrelation in interferometric radar echoes. *IEEE Transactions on Geoscience and Remote Sensing*, 30, 950–959.
- Zhang, L., Ding, X. L., and Lu, Z. (2011). Modeling PSInSAR time-series without phase unwrapping. *IEEE Transactions on Geoscience and Remote Sensing*, 49, 547–556. doi: 10.1109/TGRS.2010.2052625.
- Zhang, L., Lu, Z., Ding, X. L., Jung, H. S., Feng, G. C., and Lee, C. W. (2012). Mapping ground surface deformation using temporarily coherent point SAR interferometry—Application to Los Angeles Basin. *Remote Sensing of Environment*, 117, 429–439.